People's Democratic Republic of Algeria
Ministry of Higher Education and Scientific Research
University Hamma Lakhdar- El Oued
Faculty of Technology
Department of Electrical Engineering

Master's Thesis

Presented in Partial Fulfillment of the Requirements for the Degree of

ACADEMIC MASTER

Specialty: Electrical Networks

Theme

Optimization and Control of a Photovoltaic Water Pumping System Based on DTC of an Induction Motor

Presented by:

Brahim SAID, Hamza DIK

In front of the jury composed of:

Dr. Abdelmalek GACEM	President	Univ. El Oued	MCA
Dr. Ridha KECHIDA	Supervisor	Univ. El Oued	MCA
Dr. Youcef BEKAKRA	Reporter	Univ. El Oued	Pr

Academic year: 2025/ 2026

Acknowledgments

First and foremost, we would like to express our sincere gratitude to Allah for granting us the strength, patience, and determination to complete this work.

*We would like to extend our deepest thanks to our supervisor, **Dr. KECHIDA Ridha**, for his valuable guidance, continuous support, and constructive advice throughout this project.*

We also wish to thank the members of the jury for accepting to evaluate this work and for their valuable comments and suggestions.

Finally, we express our heartfelt appreciation to our families, friends, and all those who contributed, directly or indirectly, to the successful completion of this study.

Dedication

I dedicate this work to my parents for their constant support, encouragement, and sacrifices throughout my educational journey, May Allah protect and preserve them.

SAID Brahim

Dedication

I dedicate this work to my mother, may Allah grant her a long and healthy life, and to the memory of my father, may Allah have mercy on him.

DIK Hamza

Optimization and Control of a Photovoltaic Water Pumping System Based on DTC of an Induction Motor

Abstract: Photovoltaic Water Pumping Systems (PVWPS) are an effective and sustainable solution for water supply in remote and agricultural regions, but their performance is strongly influenced by environmental variations and control strategy efficiency. This work focuses on the modeling and performance enhancement of an induction motor-driven PVWPS using advanced MPPT and control techniques. A MATLAB/Simulink model of the PV array and DC-DC boost converter was developed, and three MPPT methods (P&O, INC, and AD-INC) were evaluated under varying irradiance and temperature. Results showed that the AD-INC method outperforms the conventional techniques by providing faster convergence, higher tracking accuracy, and lower power oscillations. For the drive system, an optimized Direct Torque Control (DTC) strategy based on a Gorilla Troops Optimizer (GTO)-tuned PI controller (PI-GTO-DTC) was proposed. The GTO algorithm was used to tune PI gains to minimize speed error and torque ripples under different operating conditions. Simulation results confirmed that the proposed PI-GTO-DTC significantly enhances system performance compared to conventional PI-DTC, resulting in reduced torque and flux ripples, smoother current waveforms, and enhanced operating stability. In general, combining AD-INC MPPT with PI-GTO-DTC leads to a more efficient, stable, and reliable PVWPS.

Keywords— Photovoltaic Water Pumping System (PVWPS), Direct Torque Control (DTC), Gorilla Troops Optimizer (GTO), PI Controller Optimization, Induction Motor, MPPT.

الملخص: تُعد أنظمة ضخ المياه الكهروضوئية حلاً فعالاً ومستداماً لتوفير المياه في المناطق النائية والزراعية، إلا أن أداءها يتأثر بشكل كبير بالتغيرات البيئية وكفاءة استراتيجية التحكم. يركز هذا العمل على نمذجة وتحسين أداء نظام ضخ يعتمد على محرك حثي باستخدام تقنيات متقدمة لتتبع نقطة القدرة العظمى (MPPT) وأساليب التحكم الحديثة. تم تطوير نموذج MATLAB/Simulink لمنظومة الخلايا الكهروضوئية ومحولة الرفع (DC–DC)، كما تم تقييم ثلاث خوارزميات MPPT وهي: الاضطراب والملاحظة (P&O)، التوصيل التفاضلي (INC)، والتوصيل التفاضلي التكيفي (AD-INC) تحت ظروف متغيرة من الإشعاع ودرجة الحرارة. أظهرت النتائج أن خوارزمية AD-INC تتفوق على الطرق التقليدية من حيث سرعة التقارب، ودقة تتبع أعلى، وتقليل التذبذبات. كما تم اقتراح استراتيجية تحكم مباشر في العزم (DTC) محسّنة تعتمد على متحكم تناسبي-تكاملي (PI) مضبوط باستخدام خوارزمية Gorilla Troops Optimizer (GTO) ضمن منهجية PI-GTO-DTC. تم استخدام خوارزمية GTO لضبط معاملات المتحكم PI بهدف تقليل خطأ السرعة وتذبذبات العزم تحت ظروف تشغيل مختلفة.أكدت نتائج المحاكاة أن استراتيجية PI-GTO-DTC المقترحة تحقق تحسناً ملحوظاً في أداء النظام مقارنة بالتحكم التقليدي PI-DTC، من خلال تحسين الاستجابة الديناميكية، وتقليل تموجات العزم والفيض، وتحسين جودة التيار، وزيادة المتانة أمام التغيرات التشغيلية. وبشكل عام، فإن دمج خوارزمية AD-INC مع PI-GTO-DTC يؤدي إلى نظام ضخ كهروضوئي أكثر كفاءة واستقراراً وموثوقية.

الكلمات المفتاحية: نظام ضخ المياه الكهروضوئية ، التحكم المباشر في العزم، خوارزمية Gorilla Troops Optimizer (GTO)، تحسين متحكم PI، المحرك الحثي، تتبع نقطة القدرة العظمى. (MPPT)

List of Figures

List of Tables

List of Abbreviations

AC: Alternating Current.
DC: Direct Current.
IM: Induction Motor.
GPV: Generator Photovoltaic.
MPP: Maximum Power Point
MPPT: Maximum Power Point Tracking.
DTC: Direct Torque Control.
FOC: Field-Oriented Control
GTO : Gorilla Troops Optimizer
P&O: Perturb and Observe.
INC: Incremental Conductance
AD-INC: Adaptive Incremental Conductance
PI: Proportional–Integral Controller
PWM: Pulse Width Modulation.
PV: Photovoltaic.
PVWPS: Photovoltaic Water Pumping System
SPWM: Sinusoidal Pulse Width Modulation.
STC: Standard Test Conditions
Kp : Proportional Gain
Ki : Integral Gain
VSI: Voltage Source Inverter.
I_{pv}: Current of the photovoltaic panel
V_{pv}: Voltage of the photovoltaic panel
P_{pv}: Power of the photovoltaic panel
I_{cc}: Short circuit current
V_{co}: Open circuit voltage
Is: the saturation current
i_{ph}: Current delivered by the cell
vph: Voltage at the output of the cell
i_d: Current flowing through the diode
v_d: Voltage across the diode
r_s: Series resistor
r_p: Parallel resistance
a: the ideality factor of Junction $1<n<3$
K_b: Boltzmann constant (1 ,38.10-23 J/K)
T: temperature of the cell in degrees kelvin
q: Electron charge ($1{,}602.10^{-19}$)
G: The illumination
G_n: The nominal illumination

V_{sabc}: Stator voltages
V_{rabc}: Rotor voltages
I_{sabc}: Stator currents
I_{rabc}: Rotor currents
Φ_{sabc}: Stator Fluxes
Φ_{rabc}: Rotor Fluxes
L_{ss} : matrix of stator inductors
L_{rr} : matrix of rotor inductors
$R_s.R_r$: Stator and rotor resistances respectively
$L_s.L_r$: Stator and rotor inductances respectively
M_{sr} : Stator-rotor mutual inductance
m_s : Mutual inductance between stator phases.
m_r : Mutual inductance between rotor phases.
θ : Flux angle
(α , β): stator Axes
P: Number of Pole Pairs
T_{em}: electromagnetic torque
J: moment of inertia of the rotating masses
f: viscous friction coefficient
Ω_r: Speed of rotation of the machine
σ: Blondel's coefficient
[A] : Transition matrix.
[B] : Command matrix.
[P] : PARK transformation matrix.
φ: The water flow (m^3/s)
H: The total height (m)
ω: Rotation speed (rad/s)
a_0 , a_1, a_2: are the coefficients given by the manufacturers.
ψ: is a constant which depends on conduit diameter and on all frictional losses of the pipe network.
H_g : is the geodesic height (m)
V_s : Effective value of the voltage.
Te : Sampling period.
S_{abc} : Boolean control values of the inverter arms.
ξ : Damping Coefficient.
T_{ref} : The reference torque,

ΔT_e : The hysteresis band of the corrector.

Table of contents

General Introduction

The increasing global demand for energy and water, combined with environmental concerns related to fossil fuel consumption, has accelerated the development of sustainable and renewable energy-based systems. Among these technologies, solar photovoltaic energy has emerged as one of the most promising solutions due to its abundance, cleanliness, and suitability for decentralized applications. In particular, photovoltaic water pumping systems (PVWPS) have gained significant attention as an effective and reliable alternative for water supply in remote, rural, and agricultural regions where access to conventional electrical grids is limited or economically unfeasible.

Despite their advantages, PV systems are inherently affected by the intermittent nature of solar irradiance and temperature variations, which directly influence their power output and overall performance. Therefore, efficient energy conversion and optimal system operation require advanced control and optimization strategies. In this context, Maximum Power Point Tracking (MPPT) techniques play a crucial role in ensuring that the photovoltaic generator operates at its optimal point under varying environmental conditions.

In addition to energy optimization, the performance of the pumping subsystem, typically driven by an induction motor, depends strongly on the effectiveness of the control strategy used for speed and torque regulation. Conventional control techniques may suffer from limitations such as torque ripples, slow dynamic response, and sensitivity to parameter variations. To overcome these challenges, advanced control methods such as Direct Torque Control (DTC) have been widely adopted due to their fast dynamic response and simple structure. However, further improvements are still required to enhance their robustness and reduce performance degradation under uncertain operating conditions.

Recently, intelligent optimization algorithms inspired by natural phenomena have been introduced to improve control system performance. Among them, the Gorilla Troops Optimizer (GTO) has demonstrated strong capability in handling complex nonlinear optimization problems. When applied to the tuning of Proportional–Integral (PI) controllers within DTC schemes, GTO can significantly enhance system dynamics, reduce tracking errors, and improve overall stability.

Based on this context, this work focuses on the modeling, control, and performance improvement of an induction motor-driven photovoltaic water pumping system. The study integrates advanced MPPT techniques with an optimized DTC strategy based on GTO-tuned

PI controllers, aiming to improve energy extraction efficiency and enhance the dynamic performance of the pumping system under variable environmental conditions.

The remainder of this thesis is organized as follows: Chapter I introduces the general background and fundamentals of PVWPS. Chapter II presents the modeling of the photovoltaic array and DC-DC boost converter along with MPPT techniques. Chapter III focuses on the modeling of the induction motor, centrifugal pump, and inverter. Chapter IV introduces the proposed PI-GTO-based DTC strategy and discusses the obtained simulation results and performance evaluation.

Chapter I
Photovoltaic Water Pumping Systems

I.1 Introduction

The growing global demand for water and energy, combined with the environmental challenges associated with conventional fossil-fuel-based systems, has accelerated the development of sustainable and renewable energy technologies. Among these technologies, photovoltaic (PV) energy has emerged as one of the most promising solutions due to its abundance, cleanliness, reliability, and decreasing installation cost. In remote and rural areas where access to the electrical grid remains limited or economically impractical, photovoltaic water pumping systems (PVWPS) provide an efficient and environmentally friendly alternative for water supply applications such as irrigation, livestock watering, domestic consumption, and industrial processes.

Photovoltaic water pumping systems operate by converting solar radiation into electrical energy through photovoltaic modules, which then drive electric motors coupled to water pumps. The continuous evolution of photovoltaic technologies, power electronic converters, electric drives, and intelligent control strategies has significantly improved the efficiency, reliability, and economic viability of these systems. In addition, recent advances in optimization algorithms and artificial intelligence techniques have enabled better energy management, enhanced maximum power extraction, fault diagnosis capabilities, and improved hydraulic performance under varying environmental conditions.

This chapter presents a comprehensive overview of photovoltaic water pumping systems and the fundamental concepts associated with their operation and development. It begins with the historical development and evolution of photovoltaic technologies, including the classification and comparison of different generations of solar cells. The chapter then discusses the structure and operating principles of photovoltaic generators and photovoltaic cells. Subsequently, the classification of photovoltaic systems and the operating principle of PV water pumping systems are presented along with their main applications and essential components. Finally, the chapter highlights the most commonly used control strategies and optimization techniques employed to enhance the performance, efficiency, and reliability of photovoltaic pumping systems.

I.2 Historical Development of Photovoltaic Technology

The historical development of PV technology can be summarized through key milestones that shaped its evolution into a mature renewable energy solution:

- ✓ 1839: Discovery of the photovoltaic effect by Alexandre Edmond Becquerel.
- ✓ 1905: Theoretical explanation of the photoelectric effect by Albert Einstein.
- ✓ 1954: First practical silicon solar cell developed at Bell Laboratories (~6% efficiency).
- ✓ 1960s: Deployment of PV technology in space missions by NASA.
- ✓ 1973: Increased global interest following the 1973 oil crisis.
- ✓ 1980s–2000s: Advancements in efficiency and cost reduction, including thin-film technologies.
- ✓ Late 2000s–present: Emergence of advanced technologies such as Perovskite solar cells and multi-junction cells, enabling higher efficiencies and broader applications.

These milestones highlight the transition of PV technology from a scientific discovery to a key component of modern sustainable energy systems.

I.3 Evolution of Photovoltaic Technologies

I.3.1 Classification of PV Technologies

Photovoltaic technologies are generally classified into three main categories: first-generation, second-generation, and third-generation, based on their material structure, efficiency, and level of technological maturity, as illustrated in Fig. (I.1).

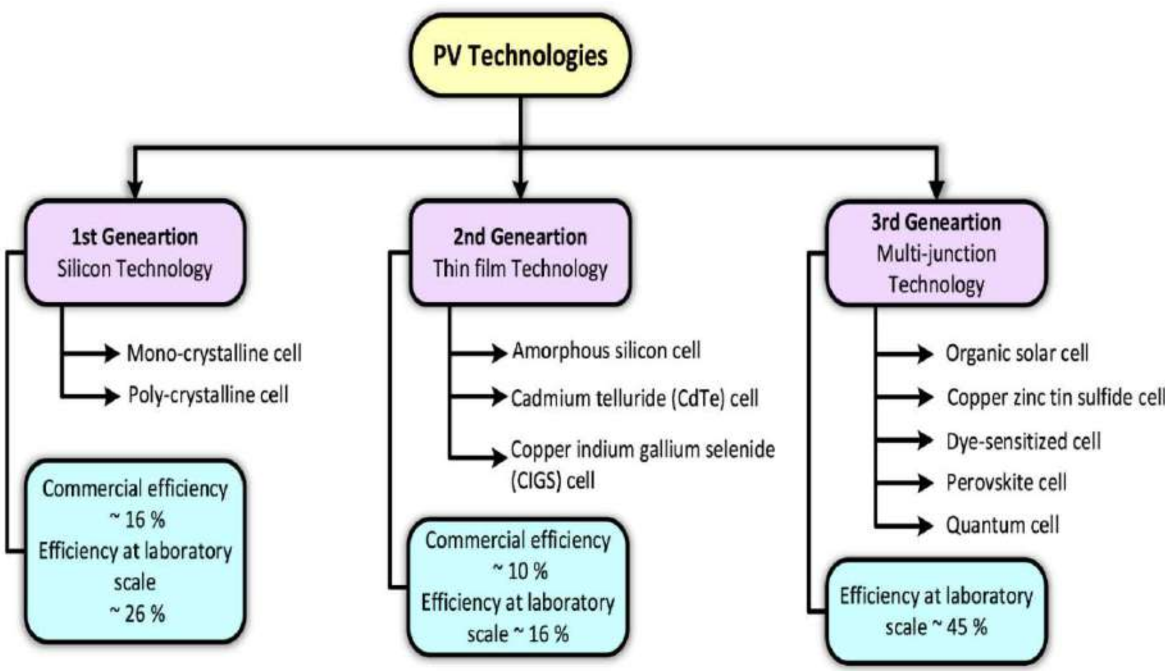

Fig. I.1: Classification of PV technologies.

I.3.1.1 First Generation: Crystalline Silicon Solar Cells

First-generation photovoltaic technologies are predominantly based on crystalline silicon, including monocrystalline and polycrystalline cells. Monocrystalline cells, made from a single high-purity crystal, offer higher efficiency (~20%) and longer lifespan (25 years) [1]. In contrast, polycrystalline cells are produced through a simpler and lower-cost process but exhibit lower efficiency (~15%) due to crystal boundaries and reduced material purity, along with slightly lower performance under high temperatures, as shown in Fig. (I.2).

Fig I.2: Crystalline silicon solar cells

Fig I.3: Thin-film solar cells

I.3.1.2 Second Generation: Thin-Film Solar Cells

Second-generation photovoltaic technologies, known as thin-film cells, include amorphous silicon (a-Si), CdTe, and CIGS. They are characterized by lower material usage and reduced production costs compared to crystalline silicon technologies. Amorphous silicon offers low efficiency (~6–8%) and is mainly used in low-power applications. CdTe provides moderate efficiency (≈9–11% commercially, up to ~16% in laboratories) with good low-light performance, but raises environmental concerns due to cadmium [2]. CIGS achieves higher efficiencies (≈13% commercially, up to ~21% in laboratories) and good performance under shading, though it is limited by material availability and environmental considerations, Fig I.3.

I.3.1.3 Third Generation:

Third-generation photovoltaic technologies aim to overcome the cost and efficiency limits of conventional silicon systems through innovative materials and concepts. Notably, Perovskite solar cells have achieved efficiencies around 20% with potential up to ~25%, along with strong performance under low-light conditions. In parallel, organic-based technologies such as dyesensitized (DSSC) and polymer solar cells (OPV) offer advantages including flexibility, lightweight design, and low-cost fabrication, though with relatively lower efficiencies.

More advanced approaches such as quantum dot cells and multi-junction devices seek to enhance performance using mechanisms like multi-exciton generation and hot carrier extraction. Despite their promising features, these technologies still face key challenges related to long-term stability, material toxicity, and large-scale commercialization, making ongoing research essential for improving their durability and practical viability [3].

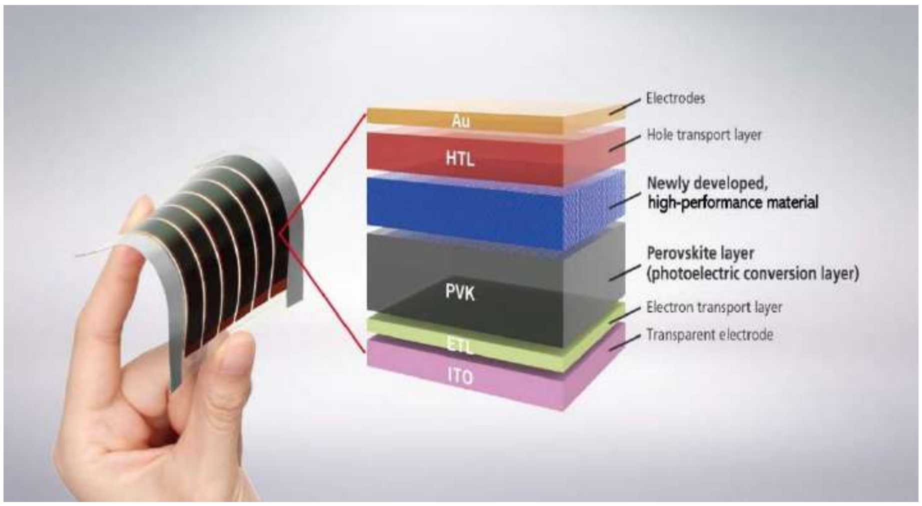

Fig I.4: Perovskite solar cells

I.3.1.4 Comparison of Photovoltaic Technologies

Table I.1: Comparison of Photovoltaic Technologies

Generation	Technology	Efficiency	Cost	Reliability
First Generation	**Monocrystalline Silicon**	High (≈ 18–24%)	High	Very high (long lifespan, ~25+ years)
	Polycrystalline Silicon	Moderate (≈15–20%)	Medium	High (slightly lower than monocrystalline)
Second Generation	**Amorphous Silicon (a-Si)**	Low (≈ 6–10%)	Low	Moderate (degradation over time)
	Cadmium Telluride (CdTe)	Moderate (≈ 9–16%)	Low	High (good stability, but environmental concerns)
	CIGS (Cu-In-Ga-Se)	Moderate–High (≈ 13–21%)	Medium	High (good performance, stable)
Third Generation	**Perovskite Solar Cells**	High (≈ 20–25% lab)	Low	Low–Moderate
	Organic Solar Cells (OPV)	Low (≈ 10–11%)	Very low	Low (short lifespan, degradation)
	Future Trends (Quantum dots, multi-junction, etc.)	Very high (potential > 30%)	Currently high (research stage)	Uncertain (still under development)

The comparison of PV technologies highlights the trade-offs between efficiency, cost, and reliability across different generations. While first-generation technologies dominate the market due to their maturity and durability, second-generation solutions focus on cost reduction, and third-generation technologies aim to achieve high efficiency with innovative, low-cost materials such as Perovskite solar cells. This classification provides a clear framework for evaluating the suitability of each technology for specific applications.

I.4 Photovoltaic Generator

A PV cell, or solar cell, is a device that converts sunlight directly into electrical energy via the photovoltaic effect. When photons are absorbed by a semiconductor, electrons are excited and generate an electric current. PV cells are the basic components of solar panels, where interconnected cells produce sufficient power for various applications, including battery charging. Today, photovoltaic technology is a key source of clean energy, widely used in residential, commercial, industrial, and large-scale electricity generation systems [4].

Fig I.5: Photovoltaic generator

1.4.1 Photovoltaic Cell

Silicon remains the most widely used semiconductor in photovoltaic cells due to its high efficiency in converting solar energy into electricity. A photovoltaic cell is primarily based on a p–n junction, typically made of crystalline silicon, consisting of a thin n-type layer over a p-type substrate. It includes a front metallic grid for electron collection, an anti-reflective coating to enhance light absorption, and a rear metallic contact for hole collection, all protected by an encapsulation layer to ensure durability [5].

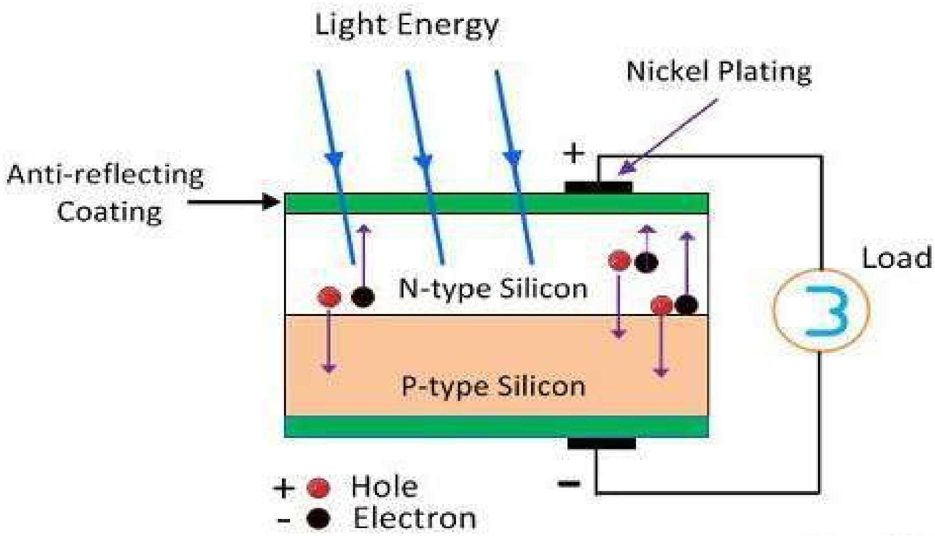

Fig I.6: Photovoltaic cell

I.4.2 Electrical Equivalent Circuit of PV Cell

The electrical behavior of a PV cell is commonly represented by an equivalent circuit consisting of a current source in parallel with a diode, along with series (R_s) and shunt (R_{sh}) resistances, Fig I.7. The current source models the generated photocurrent, the diode describes the p–n junction characteristics, while R_s and R_{sh} account for internal conduction losses and leakage currents. This model is widely employed for analysing and simulating PV cell performance [6].

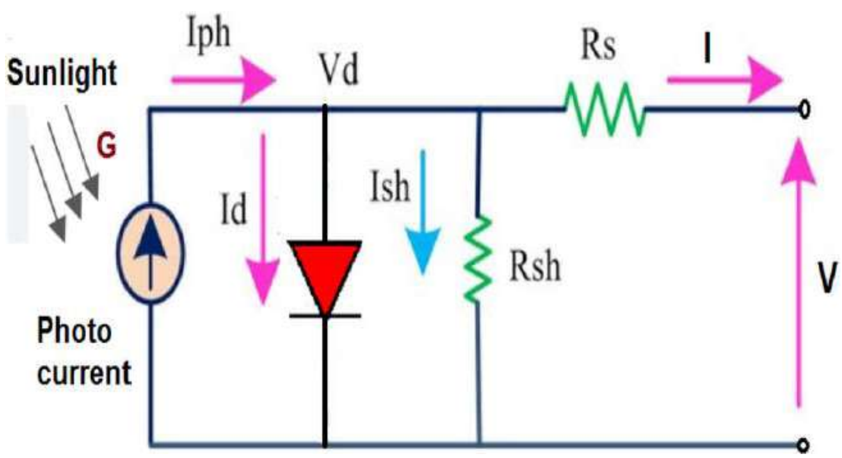

Fig I.7: Caption PV cell single-diode equivalent circuit model

I.4.3 Photovoltaic Module

A PV module is composed of interconnected solar cells arranged in series and/or parallel to deliver the required electrical output. It is protected by a transparent front glass layer for light transmission and durability, and a rear layer that provides insulation and mechanical strength.

To improve reliability, bypass diodes are used to reduce the effects of partial shading, while blocking diodes prevent reverse current flow. PV modules are characterized by key parameters such as peak power, I–V curve, open-circuit voltage (V_{oc}), short-circuit current (I_{sc}), and maximum power point (P_{mpp}, V_{mpp} and I_{mpp}), in addition to efficiency and fill factor, which indicate overall performance quality [7].

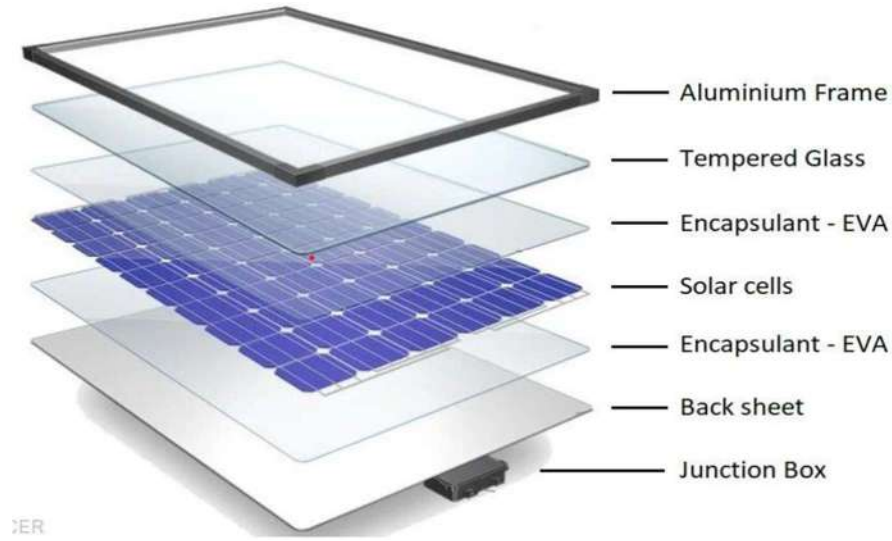

Fig I.8: Photovoltaic module components

I.4.4 Photovoltaic Panel

A PV system is composed of solar modules made up of interconnected cells, which are the basic units of energy conversion. Each cell produces a small power output with a voltage of less than 1V, and system performance is typically expressed by peak power (Wp) under standard test conditions (1 kW/m², 25°C) [8]. Cells are connected in series to increase voltage and in parallel to increase current, while the generated power depends on the module surface area. PV module efficiency, defined as the ratio of electrical output to incident solar energy, generally ranges from 15% to 25%. Additionally, durability is ensured through protective front glass and sealed rear layers.

I.4.5 Photovoltaic Array

A PV array is composed of multiple PV modules interconnected in series and/or parallel configurations to provide the required voltage and current for a given application. The size of a PV array can vary significantly, ranging from a small setup with only a few modules to large-scale installations covering extensive areas, depending on the energy demand [9].

I.5 Classification of Photovoltaic Systems

Photovoltaic systems are classified into three main types in Fig I.9, grid-connected, stand-alone (off-grid), and hybrid systems, depending on their connection to the utility grid and use of energy storage or additional power sources.

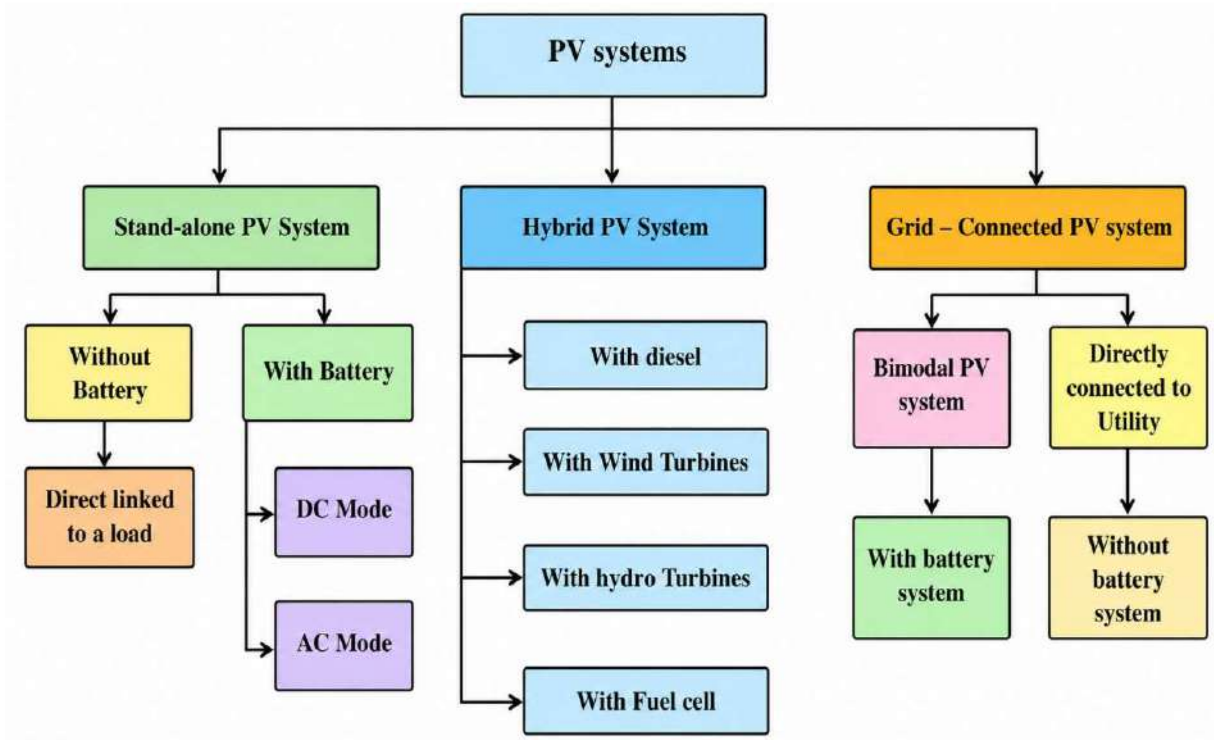

Fig I.9: Classification of photovoltaic systems

I.5.1 Grid-Connected PV Systems

A grid-connected PV system operates in conjunction with the utility grid, allowing the export of excess electricity. It mainly consists of PV modules, an inverter for DC/AC conversion, and a grid interface for safe connection [10]. These systems are classified into two main types:

- Total injection: all generated energy is fed into the grid.
- Surplus injection: energy is first used locally, and any excess is exported to the grid.

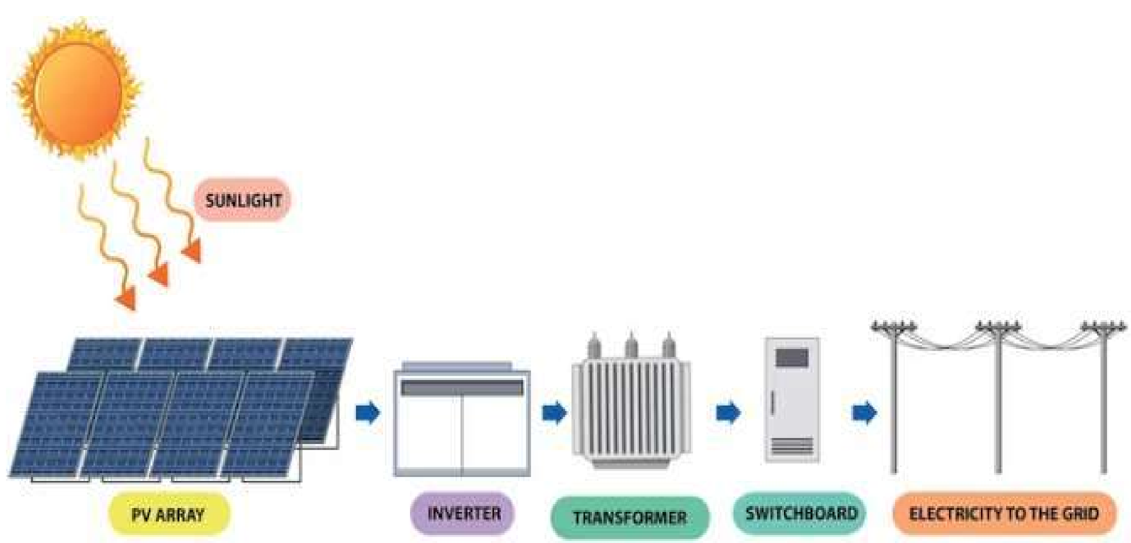

Fig I.10: Grid-connected PV systems

I.5.2 Stand-alone PV Systems

Stand-alone PV systems operate independently of the utility grid and are mainly used in remote areas. To ensure continuous power despite solar intermittency, they rely on battery storage to store excess energy [11]. These systems typically include PV modules, a charge controller, a battery bank, and an inverter when AC power is required.

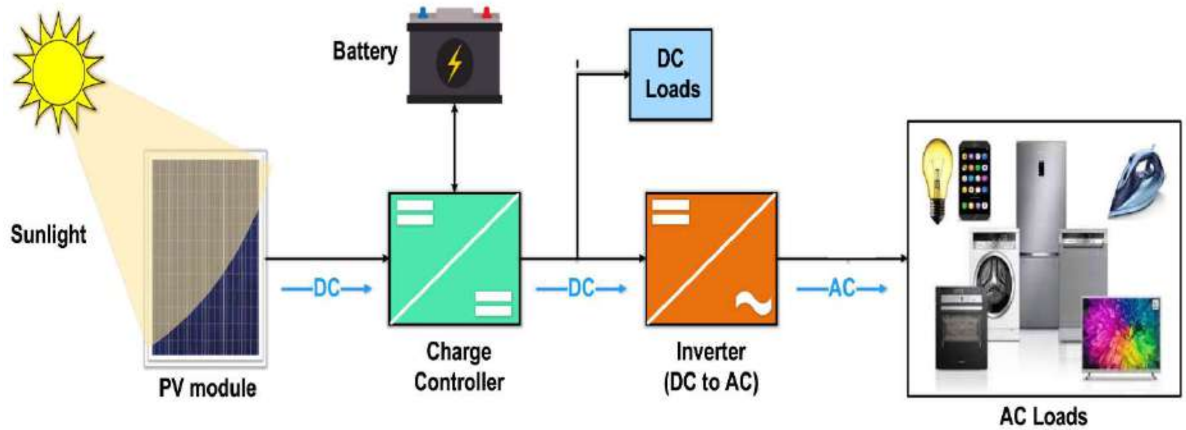

Fig I.11: Stand-alone PV systems

I.5.3 Hybrid PV Systems

Hybrid PV systems operate independently of the grid by combining multiple energy sources, such as solar panels, wind turbines, or generators, to enhance reliability. Energy storage is integrated to ensure continuous power supply and meet high-demand applications. This configuration enables efficient management of energy production and storage, providing a stable and balanced output [12].

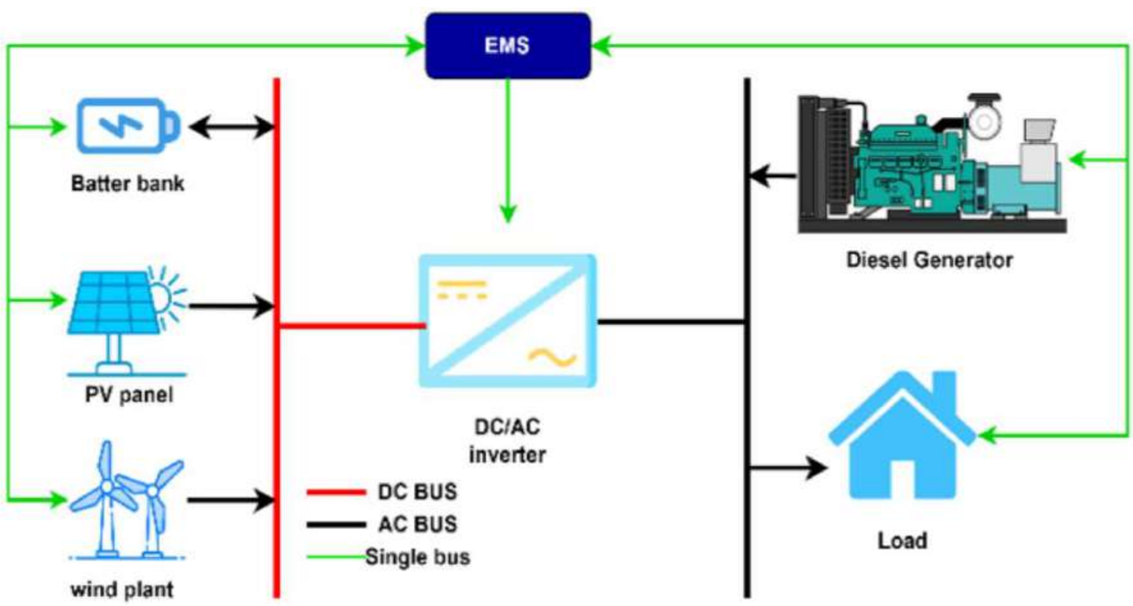

Fig I.12: Hybrid PV systems

I.6 Photovoltaic Water Pumping Systems

Photovoltaic water pumping systems represent a sustainable and cost-effective solution for water supply, particularly in remote and arid regions where access to conventional energy sources is limited. By directly converting solar energy into electrical power to drive water pumps, these systems eliminate the need for fuel and reduce operational costs and environmental impact. Their flexibility, low maintenance requirements, and compatibility with various storage strategies (electrical or hydraulic) make them increasingly attractive for agricultural irrigation, livestock watering, and rural water supply applications.

I.6.1 Principle of PV Water Pumping

The principle of photovoltaic water pumping is based on converting solar radiation into electrical energy using PV modules to drive an electric motor coupled to a water pump. The generated power may be used directly or regulated through power conditioning devices (such as converters or controllers) to match the pump requirements. The water is then pumped and stored in tanks or reservoirs, ensuring availability even when solar energy is not present.

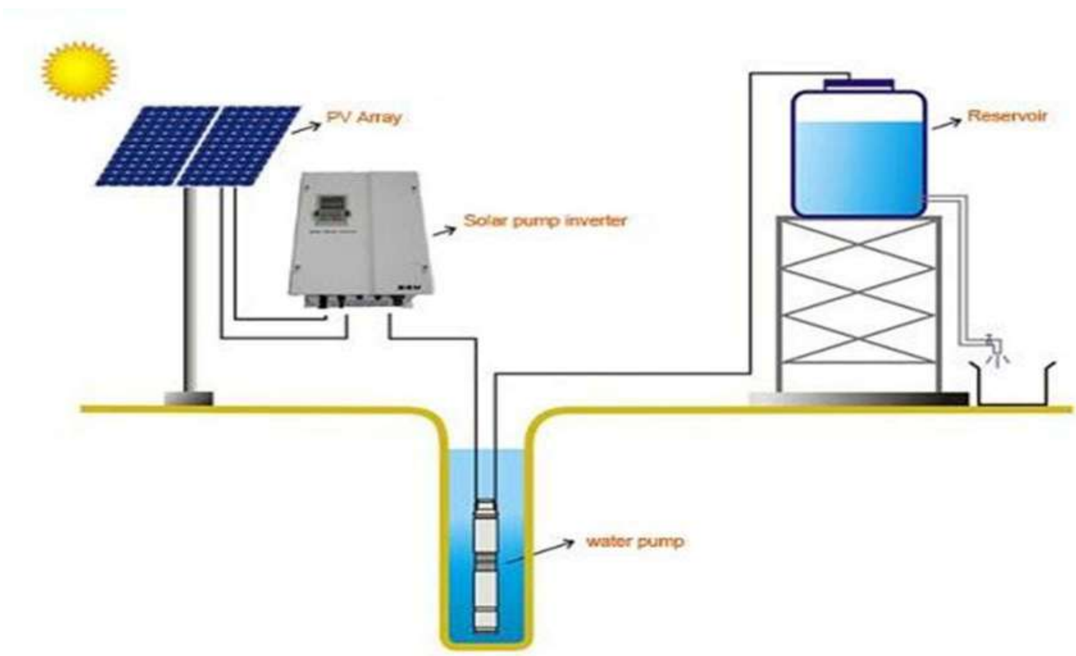

Fig I.13: PV water pumping

I.6.2 Applications of PV Pumping Systems

Centrifugal pumps are widely used in PV pumping systems due to their simplicity, low cost, and adaptability to various operating conditions. Their main applications include irrigation, water supply, hydroelectric installations, water storage systems, and petroleum-related processes [13].

However, they are not suitable for pumping highly viscous or shear-sensitive fluids, nor for precise metering tasks, where positive displacement pumps are preferred. Despite these limitations, centrifugal pumps remain advantageous for handling fluids containing suspended solids.

I.6.3 Components of Photovoltaic Water Pumping System

A photovoltaic (PV) water pumping system generally consists of the following main components:

- **PV generator (solar array)**
- **DC/DC converter (boost converter)**
- **DC/AC converter (inverter)**
- **Motor-pump unit**

The performance of a solar water pumping system depends on both site-specific factors and equipment-related parameters. Site-specific characteristics include solar irradiation, ambient temperature, and geographical location. Equipment-related factors involve the efficiency, reliability, and service life of the system components.

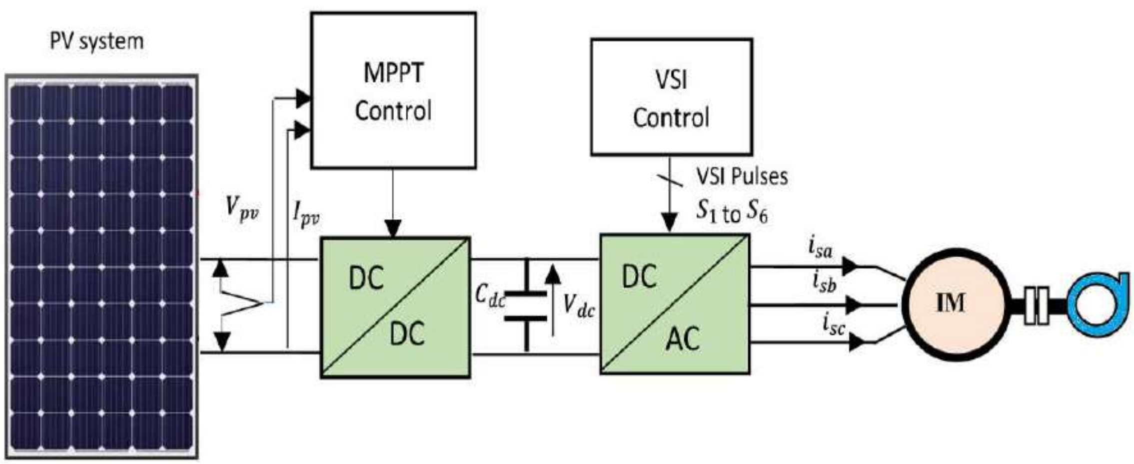

Fig. I.14: Components of photovoltaic water pumping system

I.7 Control Techniques used in PV Pumping Systems

Control techniques in photovoltaic (PV) pumping systems are essential for optimizing energy extraction and ensuring reliable operation under varying environmental conditions. Due to the variability of solar energy, adaptive control strategies are required to respond to changes in irradiance, temperature, and load. MPPT is the primary method used to maximize the output of the PV array, with common algorithms such as P&O and Incremental Conductance. In addition, motor-pump control techniques regulate system performance, where simple methods like V/f control are widely used, while advanced approaches such as Field-Oriented Control (FOC) and Direct Torque

Control (DTC) offer improved efficiency and dynamic response [14]. Overall, combining MPPT with advanced motor control enhances the efficiency, stability, and reliability of PV pumping systems.

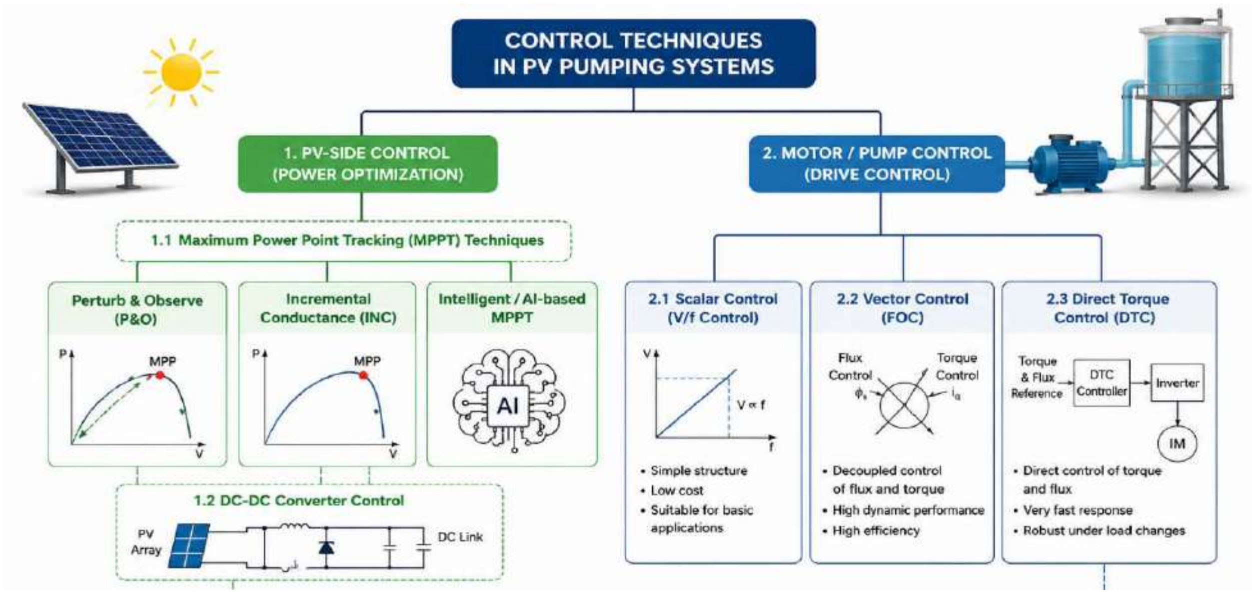

Fig I.15: Control techniques used in PV pumping systems

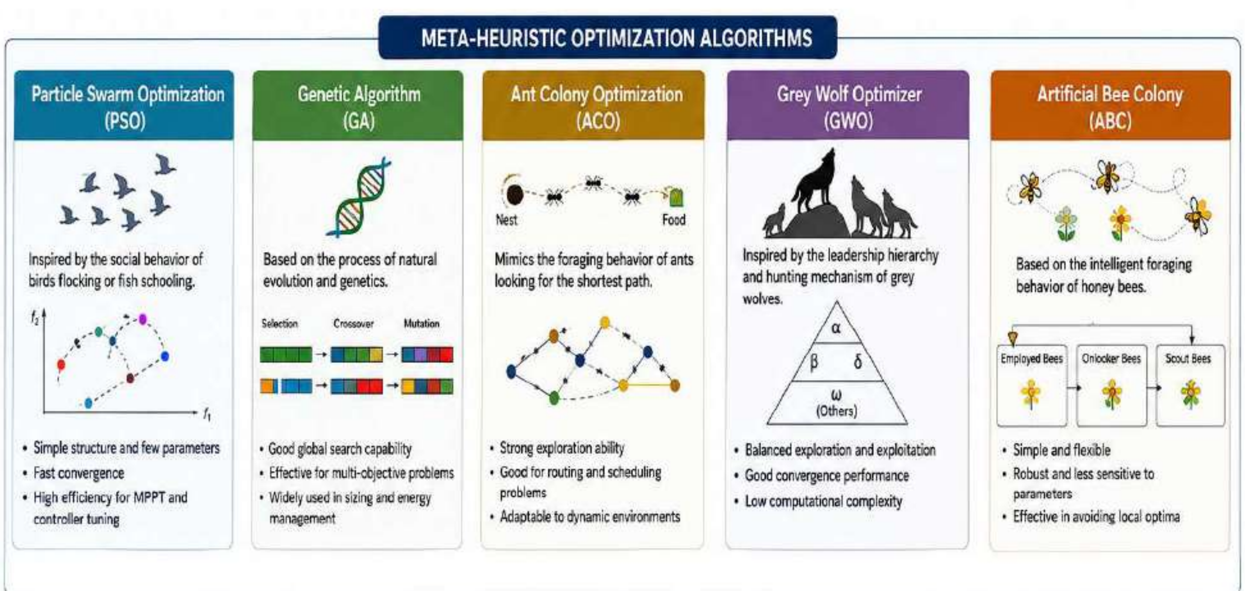

Fig I.16: Optimization techniques algorithms

I.8 Optimization Techniques in Photovoltaic Pumping Systems

Optimization techniques in PV pumping systems are widely used to improve energy efficiency, maximize water delivery, and enhance overall system performance under varying environmental conditions. These techniques aim to determine the optimal operating parameters of the PV array, power converters, motor–pump unit, and control system while minimizing energy losses and operational costs. Meta-heuristic algorithms such as Particle Swarm Optimization (PSO), Genetic Algorithm (GA), Ant Colony Optimization (ACO), Grey Wolf Optimizer (GWO), and Artificial Bee Colony (ABC) are extensively used for MPPT optimization, controller tuning, energy management, and pump scheduling. These methods provide high accuracy, fast convergence, and improved robustness compared to traditional techniques [15].

I.9 Conclusion

This chapter provided a comprehensive overview of photovoltaic water pumping systems by introducing their fundamental concepts, technological evolution, operating principles, and principal components. The historical development and classification of photovoltaic technologies highlighted the significant progress achieved in terms of conversion efficiency, cost reduction, operational reliability, and long-term sustainability, which has contributed to the widespread adoption of solar energy in water pumping applications.

In addition, the chapter examined the operating mechanism of photovoltaic generators and the overall architecture of photovoltaic water pumping systems, with particular emphasis on the interaction between PV arrays, power electronic converters, electric drives, and hydraulic pumps. Various applications of PV pumping systems were also presented, especially in remote and agricultural areas where conventional energy sources remain either unavailable or economically unfavourable. Moreover, advanced control methods and optimization techniques were discussed due to their crucial role in enhancing maximum power extraction, improving system dynamic response, minimizing energy losses, and ensuring stable and efficient operation under varying climatic and load conditions.

This foundational overview constitutes the theoretical and analytical basis for the next chapter, in which the previously presented concepts and operating principles will be formulated through detailed mathematical modeling and simulation approaches in order to evaluate the performance, efficiency, and dynamic behavior of photovoltaic water pumping systems under varying environmental and operating conditions.

Chapter II

Modeling of the PV Array and Boost Converter with MPPT Control

II.1 Introduction

Photovoltaic (PV) systems represent a highly promising approach for achieving clean and sustainable energy production, as they convert solar radiation directly into electrical energy through the photovoltaic effect. Nevertheless, ensuring optimal efficiency and performance requires precise mathematical modeling of both the PV modules and the associated DC-DC power converters.

Mathematical modeling constitutes a fundamental initial step in the design of any photovoltaic pumping system, as it provides the essential basis for system sizing, optimization, and simulation processes. The system considered in this study is a photovoltaic water pumping system, which mainly consists of a PV generator, static power converters, and a motor-pump assembly.

This chapter is devoted to the development and modeling of a photovoltaic (PV) system composed of a PV array coupled with a boost converter and controlled using MPPT techniques. The main objective is to improve the overall efficiency of the PV system by implementing and comparing the Perturb and Observe (P&O), Incremental Conductance (INC), and Adaptive Incremental Conductance (AD-INC) algorithms in order to accurately track the Maximum Power Point (MPP) under varying environmental conditions, particularly changes in solar irradiance and temperature.

II.2 Modeling of Photovoltaic System

The PV panel is commonly modeled using the single-diode equivalent circuit due to its simplicity and satisfactory accuracy, Fig II.1. This model consists of a photocurrent source I_{ph}, a diode, a series resistance R_s, and a shunt resistance R_{sh}. The output current of the PV cell can be expressed as:

$$I_{pv} = I_{ph} - I_d - \frac{V_{pv}}{R_{sh}} = I_{ph} - I_s\left[\exp\left(\frac{q(V_{pv}+R_sI_{ph})}{ak_bT}\right)-1\right] - \frac{V_{pv}+R_sI_{ph}}{R_{sh}} \tag{II-1}$$

where I_s is the diode saturation current, q is the electron charge, k_b is the Boltzmann constant, T is the cell temperature, and n is the diode ideality factor.

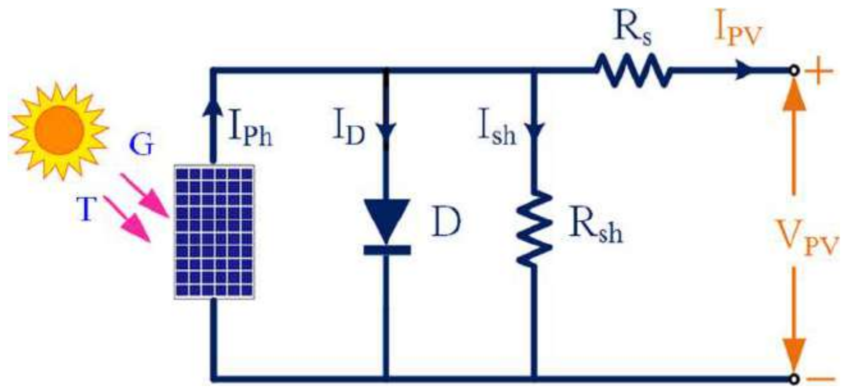

Fig. II.1: Equivalent electrical circuit of the single-diode

II.3 Characteristic of a Photovoltaic Panel

The studied PWPS is based on a solar array composed of 15 photovoltaic modules connected in series. This configuration was carefully selected to ensure a suitable match between the power generated by the PV generator and the operating requirements of the load. Table II.1 presents the main electrical characteristics of the photovoltaic modules used in this study. Under standard irradiance conditions, the array is capable of delivering approximately 4.87kW, which ensures sufficient energy to supply a 4kW rated IM driving a centrifugal water pump with efficient and stable operation.

Table II.1: Characteristic of a photovoltaic panel

Parameters	**1 panel**	**PV array**
Maximum power (P_{mpp})[W]	325	4875
Maximum current (I_{mpp})[A]	9.01	9.01
Maximum voltage (V_{mpp})[V]	36.07	541.05
Open circuit voltage (V_{oc})[V]	45.35	680.25
Short circuit current (I_{sc})[A]	9.38	9.38

II.3.1 Effect of Irradiance and Temperature on PV Characteristics

Fig. II.2 and II.3 illustrate the (V–I) and (V–P) characteristics of the PV array under varying irradiance and temperature conditions. Each operating condition generates a distinct characteristic curve associated with a specific maximum power point (V_{MPP}, I_{MPP}). These results highlight the nonlinear behavior of photovoltaic generators and demonstrate the importance of an efficient MPPT strategy to continuously ensure operation at the optimal operating point under changing environmental conditions.

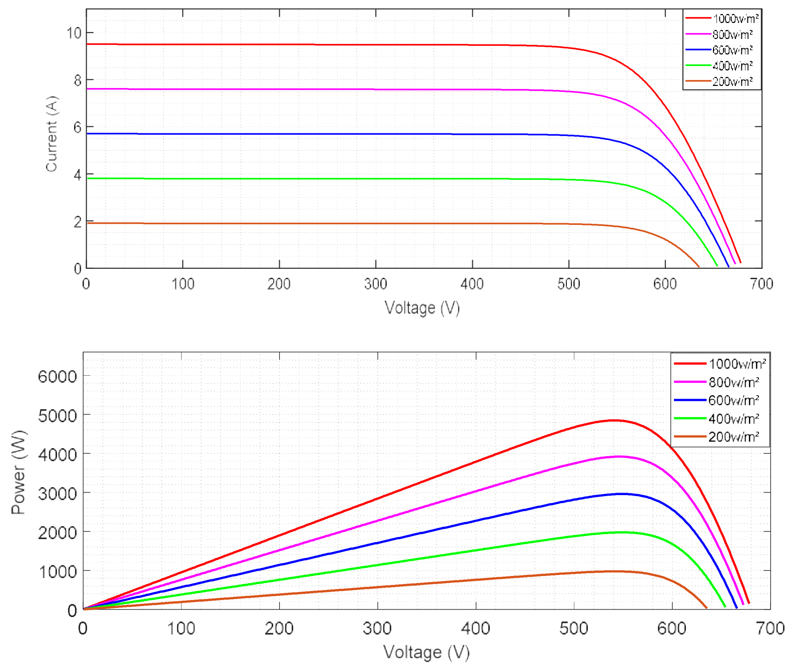

Fig. II.2: I–V and P–V characteristics under variable irradiance conditions

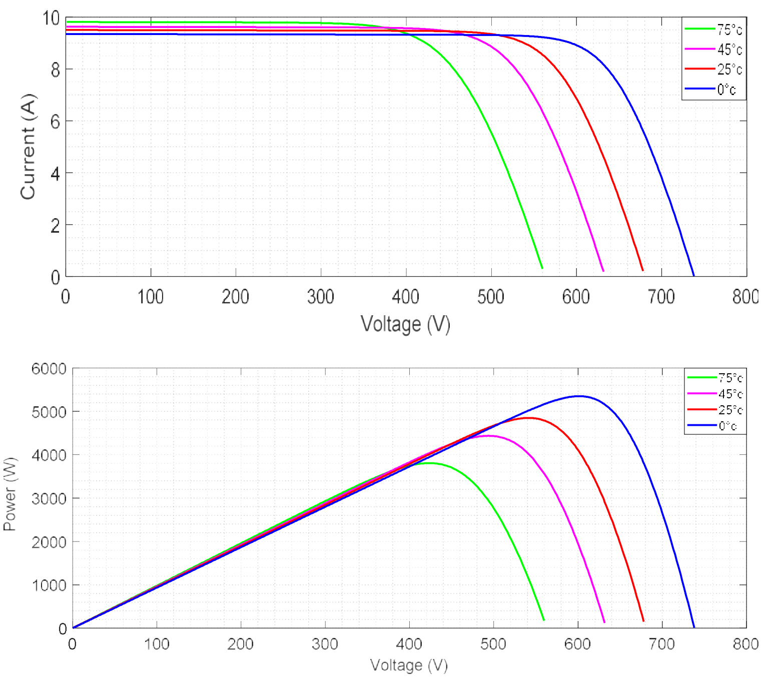

Fig. II.3: I–V and P–V characteristics under varying temperature conditions

II.4 Modeling of Boost Converter

A boost converter, also known as a step-up converter, is a DC–DC power converter designed to increase the input voltage to a higher output voltage level. Fig. II.4 illustrates the electrical circuit of the boost converter. During the first interval (αT), the switching transistor (S) is turned on, allowing the inductor current to increase gradually. As a result, the inductor (L) stores energy in its magnetic field throughout this period. At the end of this interval, the transistor (S) is turned off. Consequently, the inductor opposes the sudden decrease in current by inducing a voltage across its terminals. This induced voltage adds to the input source voltage, and the combined voltage is then delivered to the load (R) through the diode (D) [16].

This section omits the fundamental relationship essential for DC–DC boost converter modeling and control, given by:

$$V_o = \frac{V_{pv}}{1-D} \quad \text{(II-2)}$$

where Vo is the output voltage, Vin is the input voltage, and D represents the duty cycle of the switching signal.

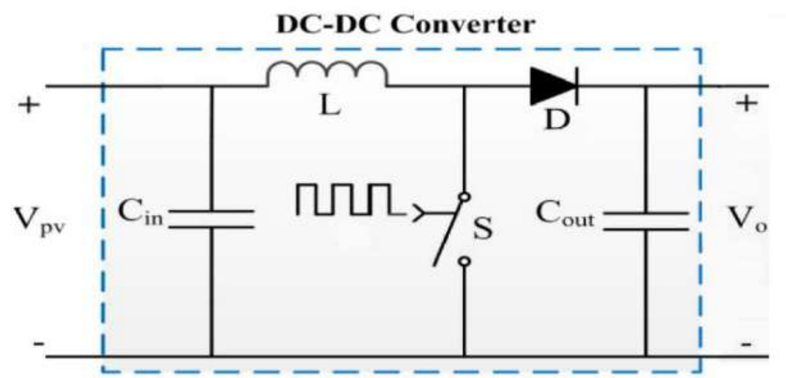

Fig. II.4: Schematic diagram of DC–DC boost converter

II.4.1 Equivalent Mathematical Model

The following figure II.5.a and b represent the modeling of the closed and open boost converters.

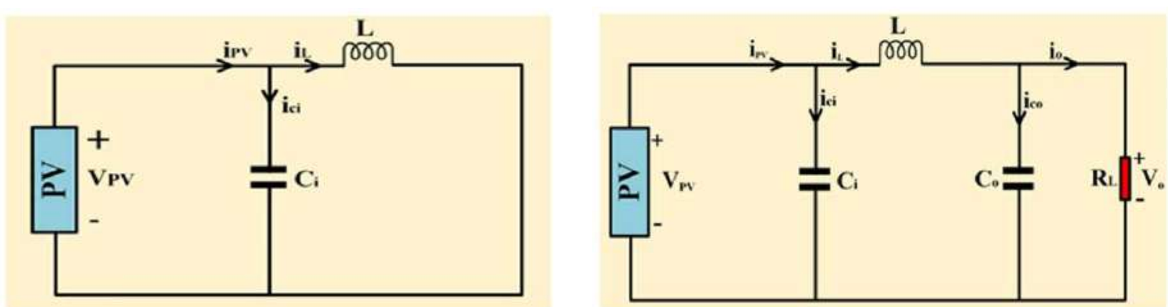

(a) (b)

Fig II.5: Schematic diagram of a closed and open boost converter

From Fig. II.5, the state space modeling is carried out as the inductor current equation is described in Eq.(II-3):

Phase 1: $T_{On} = \alpha T$

$$\frac{dV_0}{dt} = -\frac{V_0}{RC} \quad \text{(II-3)}$$

$$\frac{dI_L}{dt} = \frac{V_{pv}}{L} \quad \text{(II-4)}$$

Phase 2: $T_{Off} = (1\text{-}\alpha)T$

$$\frac{dV_0}{dt} = \frac{I_L - I_{out}}{C} \quad \text{(II-5)}$$

$$\frac{dI_L}{dt} = \frac{V_{in} - V_0}{L} \quad \text{(II-6)}$$

Using state-space averaging over one switching period, the overall system dynamics are obtained as:

$$\frac{dI_L}{dt} = \frac{V_{in}}{L} - \frac{(1-D)V_0}{L} \quad \text{(II-7)}$$

$$\frac{dV_0}{dt} = \frac{(1-D)I_L - I_{out}}{C} \quad \text{(II-8)}$$

II.5 MPPT Control

MPPT control is a fundamental technique used in photovoltaic systems to maximize the extracted power under varying irradiance and temperature conditions. Since PV characteristics are nonlinear and climate-dependent, the operating point changes continuously. Therefore, the MPPT controller adjusts the duty cycle of the DC–DC converter to maintain operation at the MPP, thereby improving system efficiency and dynamic performance. Various MPPT techniques, including P&O, INC, fuzzy logic, and neural network-based methods, have been developed to enhance tracking accuracy and energy conversion efficiency under changing environmental conditions [17].

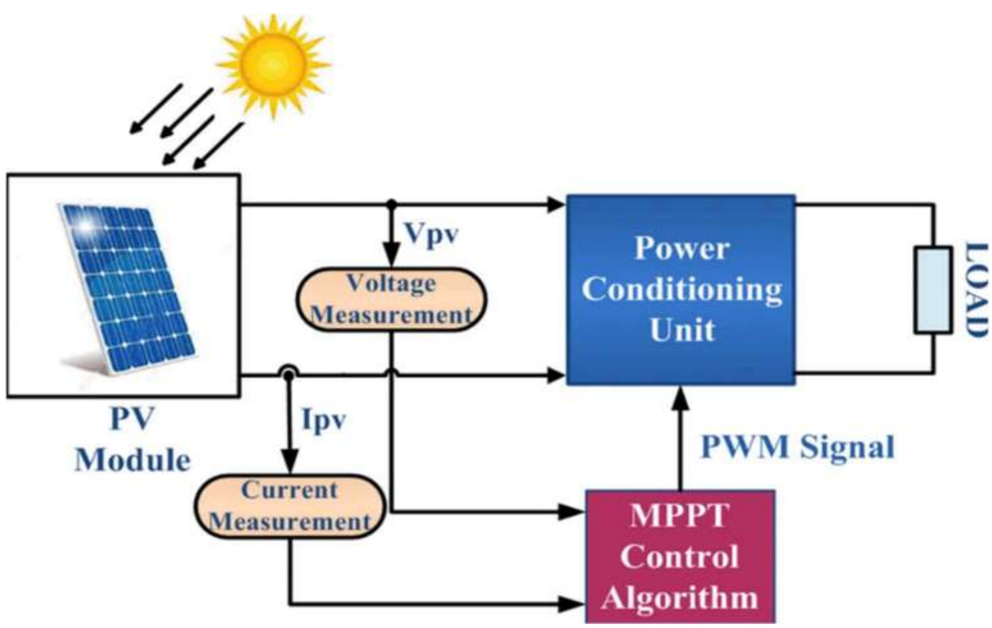

Fig II.6: Solar energy conversion chain.

II.5.1 MPPT Algorithms

Numerous MPPT algorithms have been developed, offering trade-offs between performance, complexity, and computational cost. Among them, P&O and INC are widely used due to their simplicity, but they suffer from limitations such as oscillations around the MPP, slow dynamic response, and reduced accuracy under rapid irradiance changes [18].

To address these issues, advanced techniques such as the AD-INC algorithm have been proposed, providing improved tracking accuracy, reduced oscillations, and faster convergence. Therefore, this section presents a comparative analysis of P&O, INC, and AD-INC methods in terms of operating principles and performance.

II.5.1.1 Perturb and Observe (P&O) Method

The P&O method is one of the most commonly employed techniques in MPPT research due to its simplicity and minimal implementation requirements. It relies solely on the measurement of the photovoltaic panel voltage V_{pv} and current I_{pv} enabling effective tracking of the maximum power point under varying irradiance and temperature conditions [19].

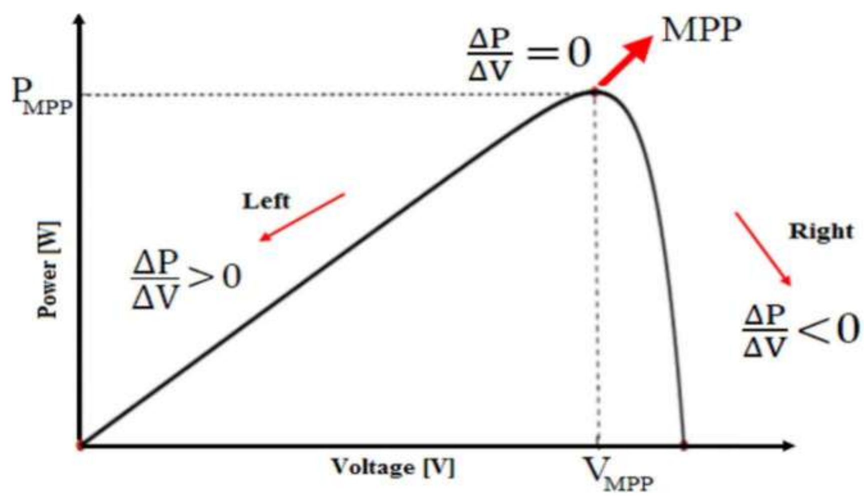

Fig II.7: Power-voltage of P&O algorithm

At steady state, when the MPP is reached, the operating voltage V_{pv} oscillates around its optimal value, which results in a certain level of power loss. This loss is directly influenced by the magnitude of the perturbation step. A larger step size enables faster dynamic response to abrupt changes in environmental conditions, but it also increases steady-state oscillations and associated power losses. Conversely, a smaller step size reduces oscillations but slows down the tracking speed, Fig. II.7. The P&O flowchart is presented in Fig. II.8.

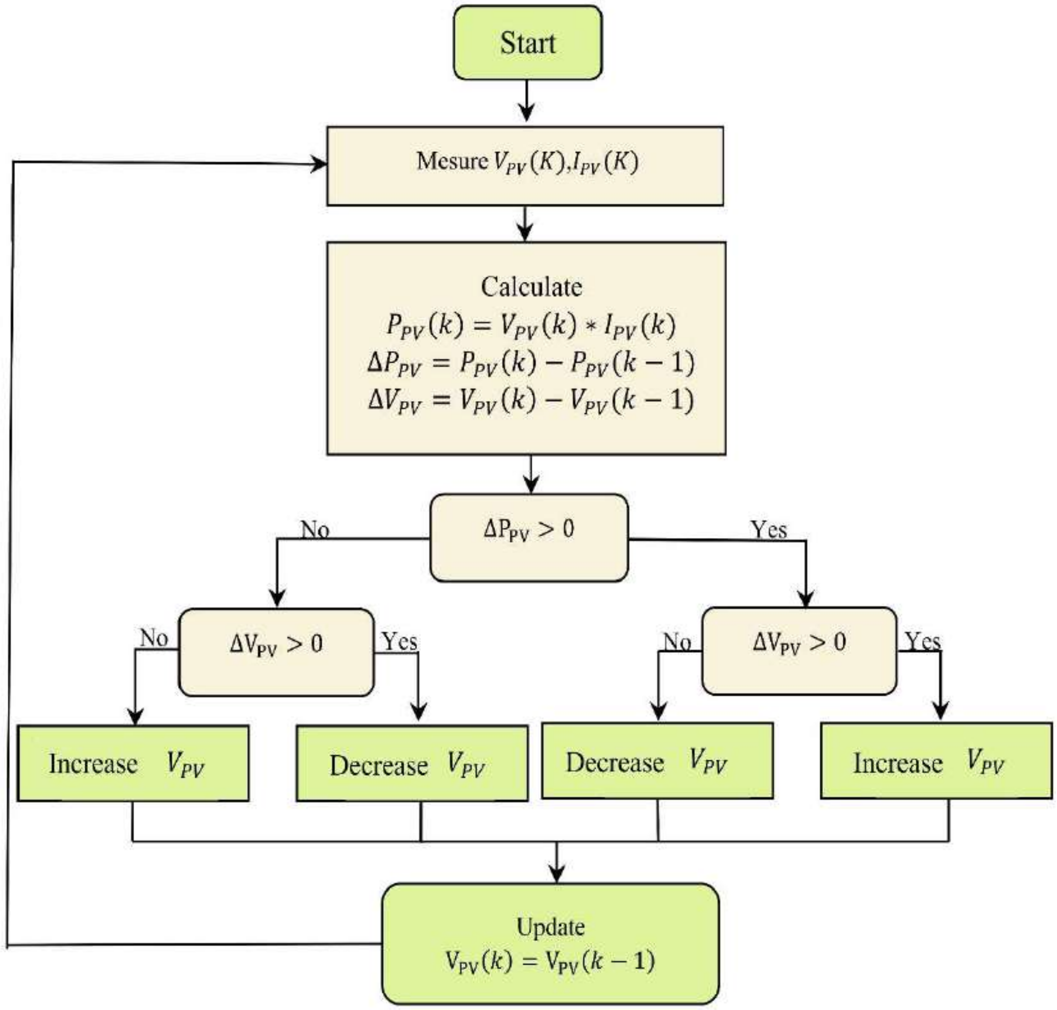

Fig II.8: Flowchart of P&O algorithm

II.5.1.2 Incremental Conductance (INC) Method

The INC algorithm is widely used to overcome the limitations of the P&O method, particularly under rapidly changing atmospheric conditions. Unlike P&O, which exhibits steady-state oscillations around the MPP, the INC method can accurately locate the MPP and stop perturbation once it is reached [20].

This algorithm determines the direction of perturbation by comparing the incremental conductance (dI/dV) with the instantaneous conductance (−I/V). This principle is based on the fact that the derivative of power with respect to voltage (dP/dV) is positive to the left of the MPP, zero at the MPP, and negative to the right (Fig. II.9). Consequently, the INC algorithm offers improved tracking accuracy and faster dynamic response under rapid irradiance changes [21]. However, these advantages come with higher computational complexity compared to the conventional P&O method. The algorithm flow is illustrated in Fig. II.10.

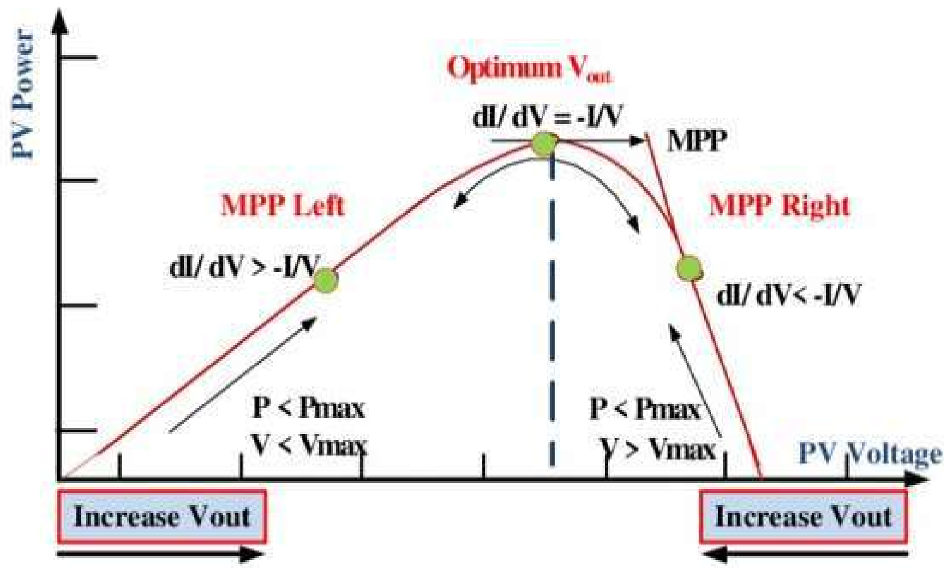

Fig II.9: PV power characteristic for different operating point.

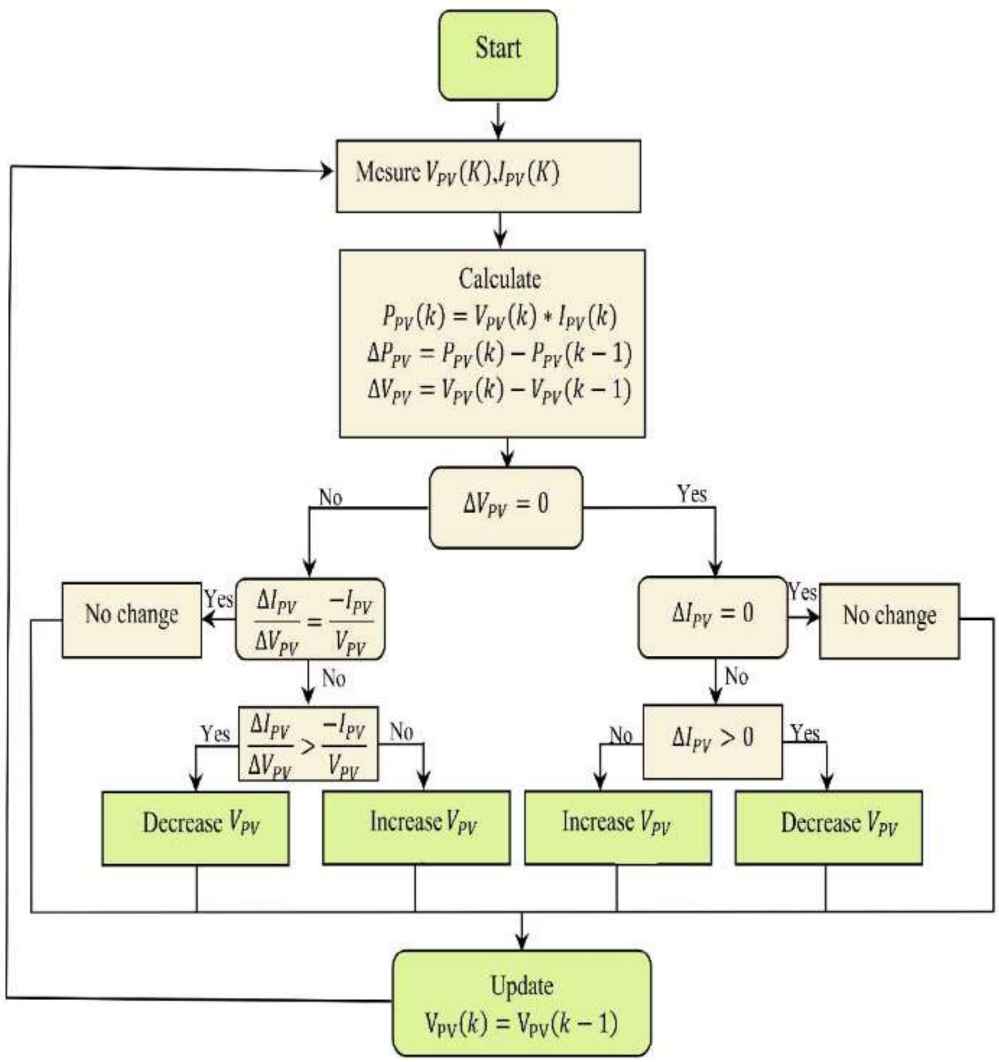

Fig II.10: Flowchart of INC algorithm

II.5.1.3 Adaptive Incremental Conductance (AD-INC) Method

To overcome the inherent limitations of the classical INC algorithm, an adaptive version is proposed in this work. The main objective is to enhance tracking speed under rapid irradiance variations while eliminating steady-state oscillations around the MPP [22]. Unlike the conventional INC method that relies on a fixed duty-cycle step, the proposed strategy introduces a variable step-size law, a stability-aware decision mechanism, and a zero-oscillation condition. The flowchart of the AD-INC algorithm is shown in Fig.II.11. The adaptive step-size is computed according to the power-voltage slope:

$$\Delta D = k_a . \left|\frac{\Delta P}{\Delta V}\right| \tag{II-9}$$

where k_a denotes the adaptive gain factor. The duty cycle is then updated according to the incremental conductance decision rule, while ensuring saturation limits D_{min} and D_{max} [23].

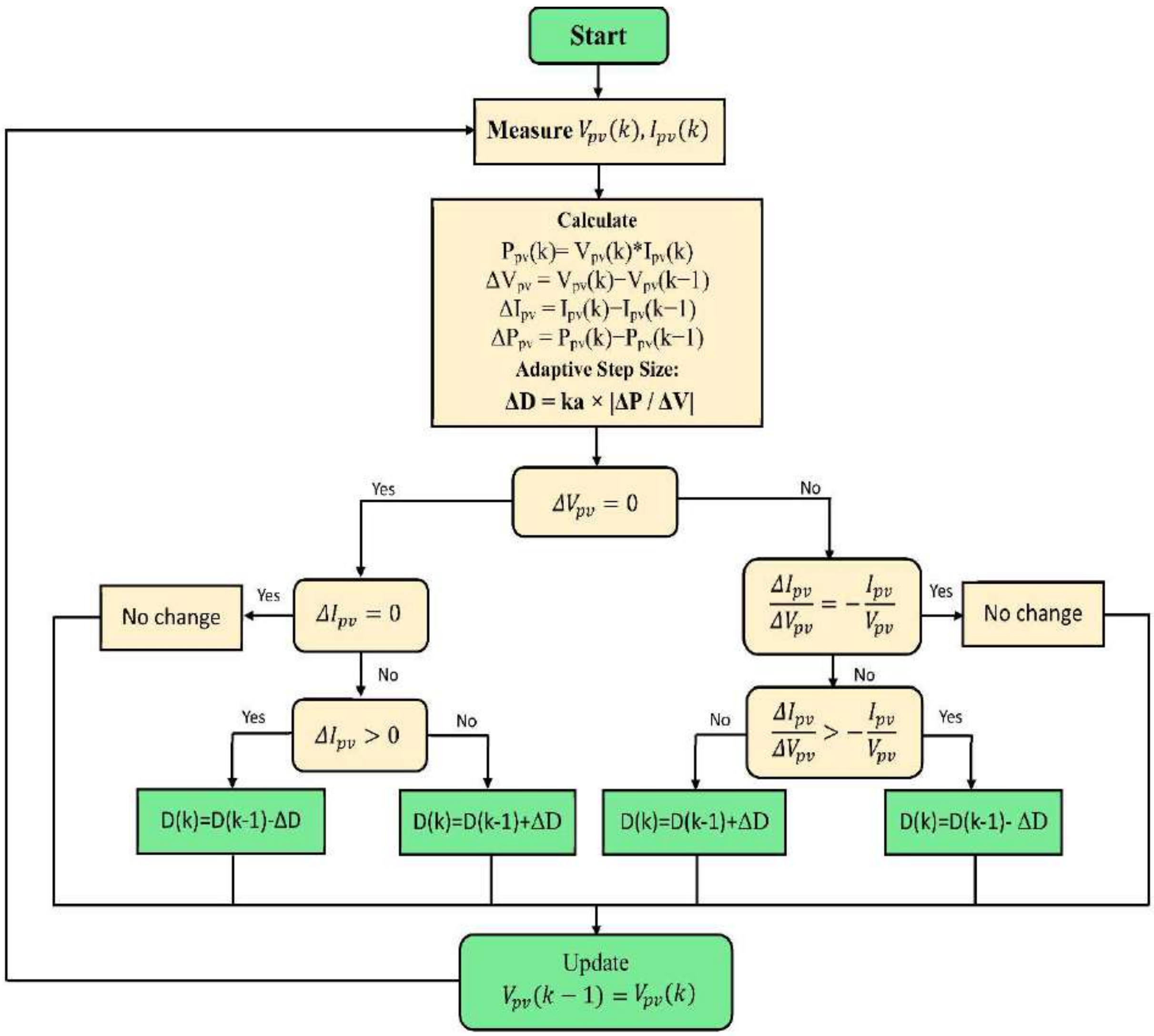

Fig II.11: Flowchart of AD-INC algorithm

II.6 Results and Discussion

To evaluate and compare the performance of the proposed MPPT techniques, a comprehensive simulation study is carried out using the MATLAB/Simulink environment. The photovoltaic system is modeled under varying irradiance and temperature conditions in order to assess the dynamic behavior and tracking capability of the considered algorithms. The comparative analysis focuses on the conventional P&O, INC, and AD-INC methods in terms of tracking accuracy, convergence speed, steady-state oscillations, and overall energy extraction efficiency. The obtained simulation results provide a clear evaluation of the effectiveness and robustness of each MPPT strategy under transient operating conditions.

II.6.1 Comparison of MPPT Algorithms under Varying Irradiance Levels

Fig. II.12 illustrates the dynamic response of the PV system under varying irradiance conditions using the P&O, INC, and AD-INC MPPT algorithms.

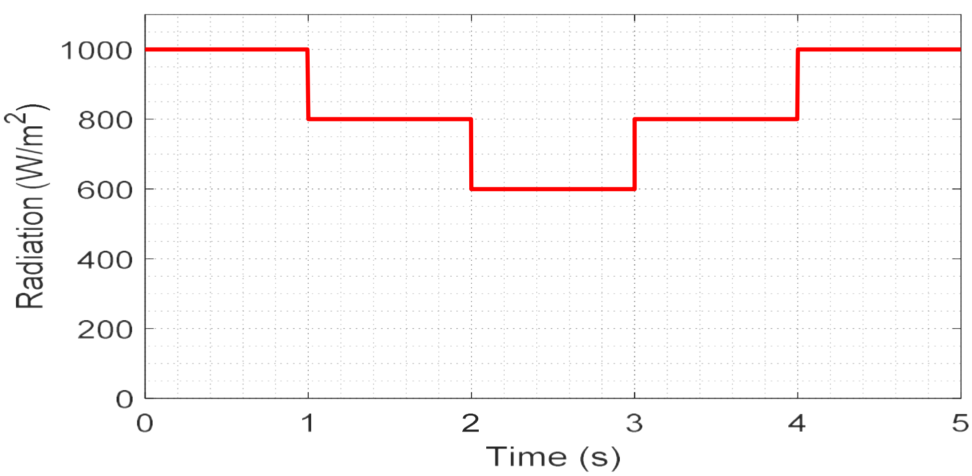

Fig II.12: Solar irradiance profile (W/m²)

The results presented in Fig. II.13 clearly indicate that the conventional P&O algorithm exhibits significant oscillations around the MPP, resulting in power fluctuations and energy losses during steady-state operation. In comparison, the INC algorithm demonstrates improved tracking performance by reducing oscillatory behavior and providing a more accurate estimation of the operating point through the relationship between incremental and instantaneous conductance. Furthermore, the proposed AD-INC algorithm achieves the best overall performance among the tested methods. It is characterized by faster convergence, reduced settling time, smoother voltage and current transitions, and markedly lower steady-state oscillations. This superior behavior is mainly attributed to the adaptive adjustment of the tracking step size, which enables rapid response to sudden irradiance variations while maintaining stable operation near the MPP. Consequently, the AD-INC technique ensures enhanced dynamic performance and significantly higher energy extraction efficiency compared to both conventional P&O and INC methods.

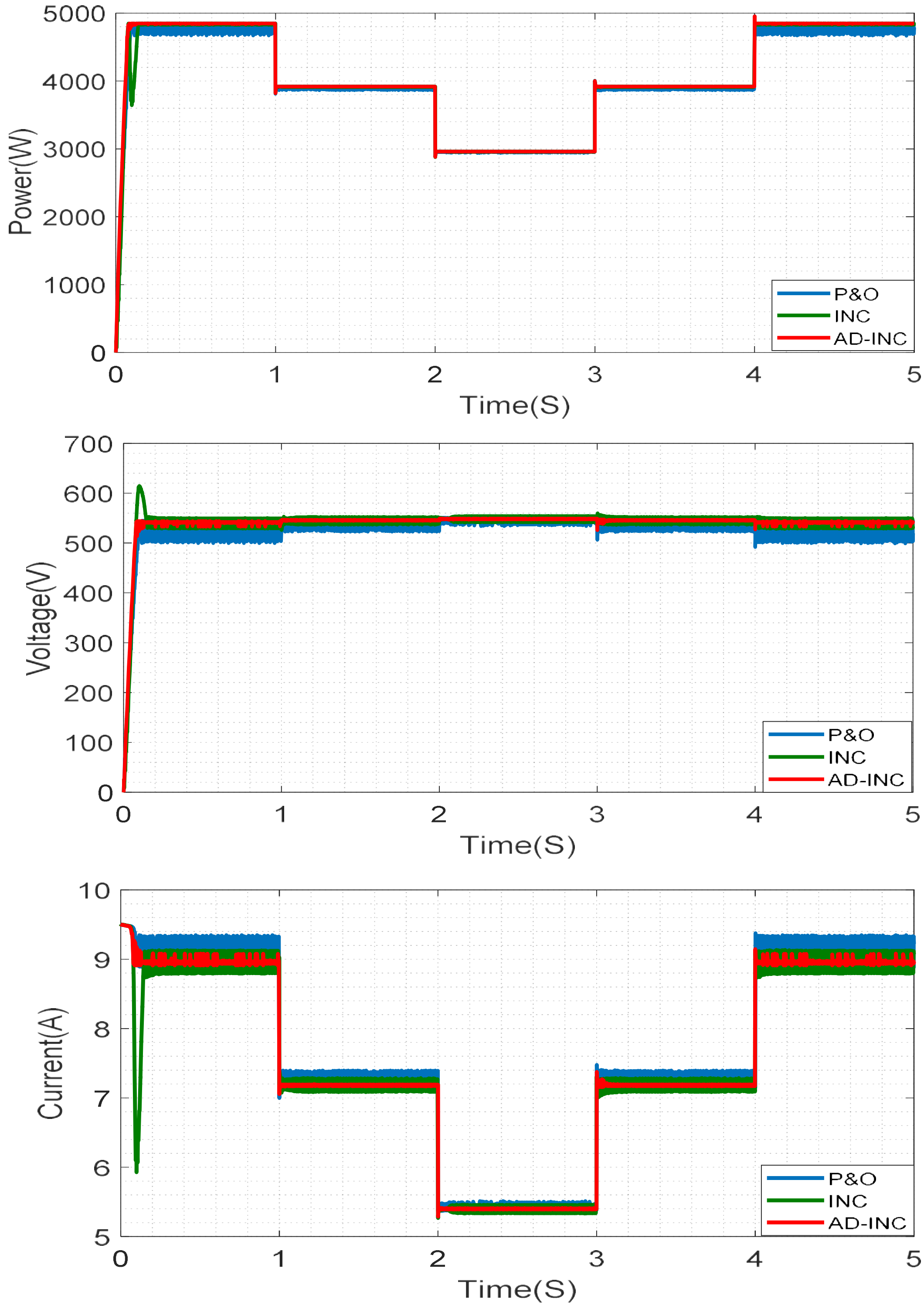

Fig II.13: PV power, voltage, and current responses under varying irradiance levels

II.6.2 Comparison of MPPT Algorithms under Varying Temperature Levels

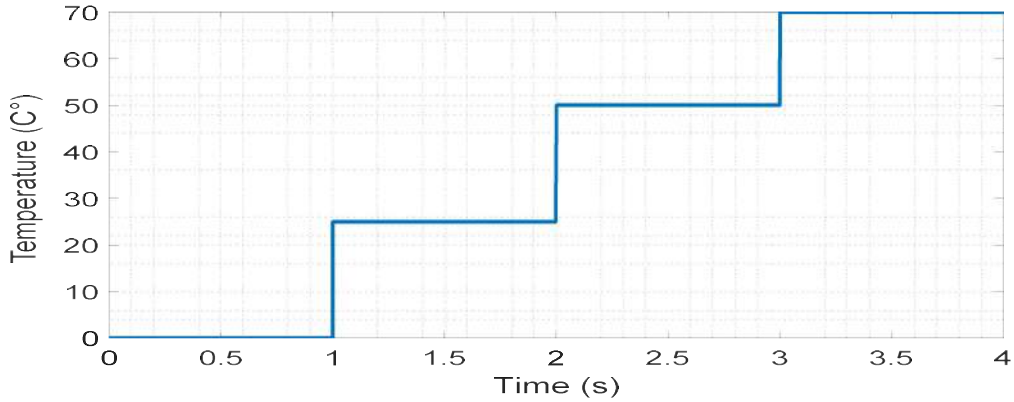

Fig. II.14: Temperature profile (°C)

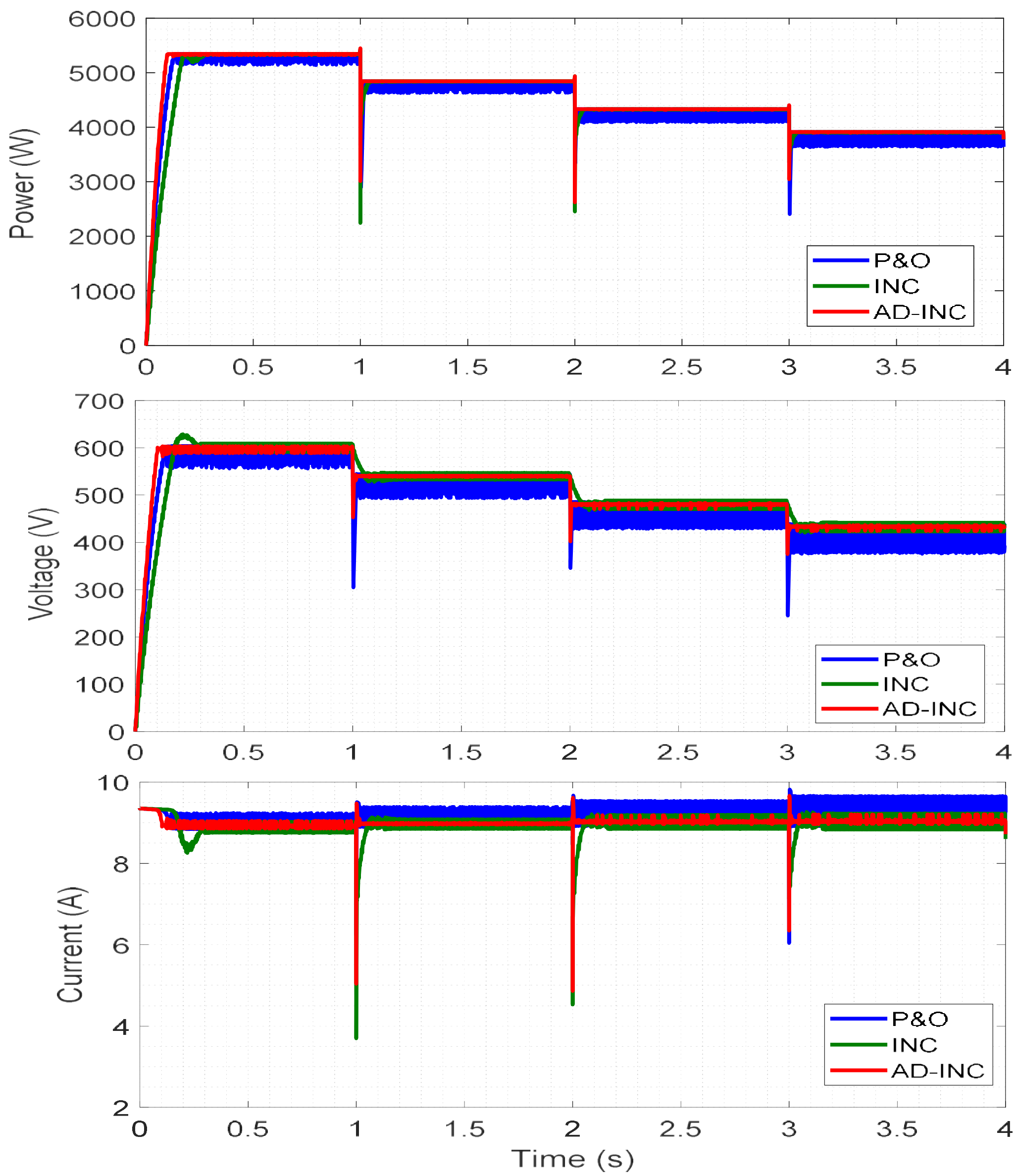

Fig. II.15: PV power, voltage, and current responses under varying temperature levels

Fig.II.14 illustrates the temperature variation profile applied to the photovoltaic system during the simulation process. This temperature profile is used to evaluate the robustness and dynamic performance of the P&O, INC, and AD-INC MPPT algorithms under varying thermal conditions. This test scenario is essential for analyzing the capability of each MPPT algorithm to maintain accurate tracking of the MPP under thermal disturbances.

Fig.II.15 illustrates the dynamic responses of the photovoltaic system under varying temperature conditions using the P&O, INC, and AD-INC MPPT algorithms. The results show that increasing temperature mainly reduces the PV output voltage and slightly decreases the maximum power. The conventional P&O algorithm exhibits noticeable oscillations and slower convergence, while the INC method improves tracking accuracy and reduces fluctuations. In contrast, the proposed AD-INC algorithm achieves the best dynamic performance with faster convergence, smoother voltage and current responses, and minimal steady-state oscillations. These results confirm the superior thermal stability and tracking efficiency of the AD-INC technique under varying temperature conditions.

The obtained results demonstrate that the proposed AD-INC algorithm significantly improves the dynamic behavior of the photovoltaic system by reducing steady-state oscillations, accelerating convergence toward the MPP, and enhancing energy extraction efficiency under rapidly changing environmental conditions. Therefore, the proposed strategy represents a promising solution for high-performance photovoltaic pumping applications.

II.7 Conclusion

In this chapter, a mathematical model of a photovoltaic system composed of a PV array and a boost converter was developed and implemented in the MATLAB/Simulink environment. Different MPPT techniques, namely P&O, INC, and AD-INC, were investigated and compared under varying irradiance and temperature conditions. The simulation results demonstrated that the conventional P&O algorithm suffers from noticeable steady-state oscillations and slower dynamic response under rapidly changing environmental conditions. The INC technique improved the tracking accuracy and reduced oscillatory behavior compared with P&O. However, the proposed AD-INC algorithm achieved the best overall performance, characterized by faster convergence speed, reduced oscillations, improved stability, and higher energy extraction efficiency. Therefore, the obtained results confirm the effectiveness and robustness of the AD-INC technique for enhancing the dynamic performance of photovoltaic systems operating under variable climatic conditions.

Chapter III.
Modeling of the Induction Motor, Centrifugal Pump, and Inverter

III.1 Introduction

The performance analysis and control of photovoltaic water pumping systems require accurate mathematical models of their main components. These models play a fundamental role in understanding the dynamic behavior of the overall system, evaluating its operating characteristics, and designing efficient control strategies under varying environmental and load conditions.

This chapter focuses on the mathematical modeling of the principal components of the proposed photovoltaic water pumping system, namely the induction motor, the centrifugal pump, and the voltage source inverter (VSI). The induction motor is modeled in the synchronous d–q reference frame in order to describe its electrical and mechanical dynamics accurately. The centrifugal pump model is developed based on the hydraulic relationships between flow rate, pressure head, and rotational speed. In addition, the inverter model is presented to describe the conversion of DC electrical power generated by the photovoltaic source into variable-frequency AC power suitable for motor operation.

III.2 Modeling of the Induction Motor

The induction motor is widely used in photovoltaic pumping systems due to its robustness, reliability, and low maintenance requirements. It converts the electrical energy supplied by the inverter into mechanical energy to drive the centrifugal pump. Accurate modeling of the induction motor is essential for analyzing its dynamic behavior and evaluating the overall system performance. In this work, the motor model is developed using the d-q reference frame, which simplifies the analysis and facilitates control implementation [24].

To simplify the mathematical modeling and analysis of the induction motor, the following assumptions are considered:

- The motor is supplied by a balanced three-phase system.
- Magnetic saturation is neglected.
- Iron losses and stray losses are ignored.
- The air gap is assumed to be uniform.

- The machine parameters are considered constant.
- The windings are sinusoidally distributed.

These assumptions allow the development of a simplified dynamic model suitable for simulation and control analysis.

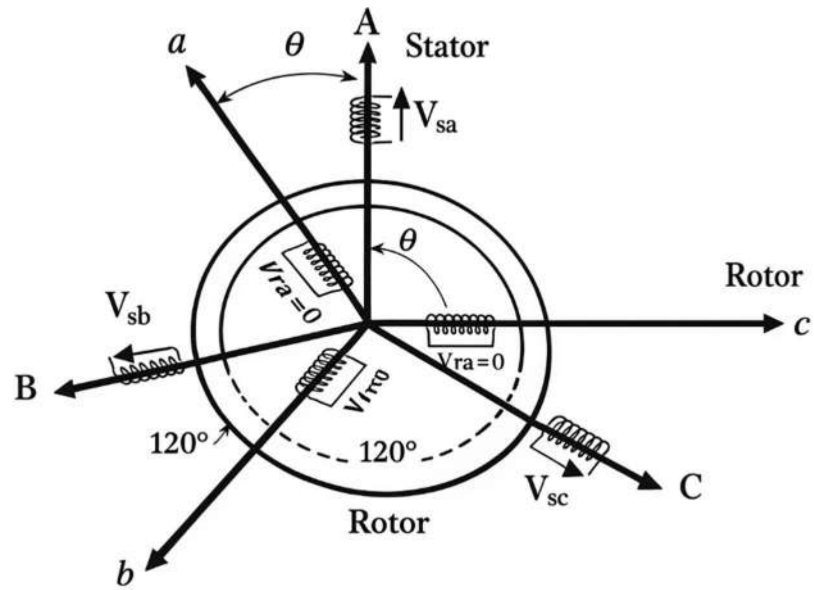

Fig III.1: Representation of the induction machine.

III.2.1 Equations of the Induction Motor

The dynamic behavior of the induction motor can be comprehensively described by three fundamental sets of equations:

III.2.2.1 Electrical Equations

By applying the generalized form of Ohm's law to each individual phase of the system:

$$\begin{cases} V_{sabc} = [R_s]\cdot[i_{sabc}] + (d/dt)\cdot[\Phi_{sabc}] \\ V_{rabc} = [R_r]\cdot[i_{rabc}] + (d/dt)\cdot[\Phi_{rabc}] \end{cases} \tag{III-1}$$

with:

$$[R_s] = \begin{bmatrix} R_s & 0 & 0 \\ 0 & R_s & 0 \\ 0 & 0 & R_s \end{bmatrix} \quad ; \quad [R_r] = \begin{bmatrix} R_r & 0 & 0 \\ 0 & R_r & 0 \\ 0 & 0 & R_r \end{bmatrix} \tag{III-2}$$

$$[V_{sabc}] = \begin{bmatrix} V_{sa} \\ V_{sb} \\ V_{sc} \end{bmatrix} \quad ; \quad [V_{rabc}] = \begin{bmatrix} V_{ra} \\ V_{rb} \\ V_{rc} \end{bmatrix} \tag{III-3}$$

$$[\Phi_{sabc}]=\begin{bmatrix}\Phi_{sa}\\ \Phi_{sb}\\ \Phi_{sc}\end{bmatrix} ; \qquad [\Phi_{rabc}]=\begin{bmatrix}\Phi_{ra}\\ \Phi_{rb}\\ \Phi_{rc}\end{bmatrix} \tag{III-4}$$

$$[i_{sabc}]=\begin{bmatrix}i_{sa}\\ i_{sb}\\ i_{sc}\end{bmatrix} ; \qquad [i_{rabc}]=\begin{bmatrix}i_{ra}\\ i_{rb}\\ i_{rc}\end{bmatrix} \tag{III-5}$$

III.2.2.2 Magnetic Equations

The relationship between the totalized fluxes on the windings and the currents can be described by the following matrix equation:

$$\begin{bmatrix}\Phi_{sabc}\\ \Phi_{rabc}\end{bmatrix}=\begin{bmatrix}[L_{ss}] & [M_{sr}]\\ [M_{rs}] & [L_{rr}]\end{bmatrix}.\begin{bmatrix}i_{sabc}\\ i_{rabc}\end{bmatrix} \tag{III-6}$$

So:

$$[\Phi_{sabc}]=[L_{ss}]\cdot[i_{sabc}]+[M_{sr}]\cdot[i_{rabc}] \tag{III-7}$$

$$[\Phi_{rabc}]=[L_{rr}]\cdot[i_{rabc}]+[M_{rs}]\cdot[i_{sabc}] \tag{III-8}$$

With: Φ_s : stator flux; Φ_r : rotor flux

$$[L_{ss}]=\begin{bmatrix}l_s & M_s & M_s\\ M_s & l_s & M_s\\ M_s & M_s & l_s\end{bmatrix}; \qquad [L_{rr}]=\begin{bmatrix}l_r & M_r & M_r\\ M_r & l_r & M_r\\ M_r & M_r & l_r\end{bmatrix} \tag{III-9}$$

$$[M_{sr}]=[M_{rs}]^t=M'_{sr}\begin{bmatrix}\cos(\alpha) & \cos(\alpha+2\pi/3) & \cos(\alpha\text{-}2\pi/3)\\ \cos(\alpha\text{-}2\pi/3) & \cos(\alpha) & \cos(\alpha+2\pi/3)\\ \cos(\alpha+2\pi/3) & \cos(\alpha\text{-}2\pi/3) & \cos(\alpha)\end{bmatrix} \tag{III-10}$$

Finally, there exists:

$$\begin{cases}[V_{sabc}]=[R_s][i_{sabc}]+(d/dt)\cdot([L_{ss}]\cdot[i_{sabc}]+[M_{sr}]\cdot[i_{rabc}])\\ [V_{rabc}]=[R_r][i_{rabc}]+(d/dt)\cdot([L_{rr}]\cdot[i_{rabc}]+[M_{rs}]\cdot[i_{sabc}])\end{cases} \tag{III-11}$$

III.2.2.3 Mechanical Equations

To analyze electromechanical transient phenomena under variable rotor speed conditions such as starting, braking, or load variations on the shaft it is necessary to incorporate the equation of motion into the system of differential equations:

$$J.\frac{d\Omega_r}{dt}=T_{em}-T_r-f.\Omega_r \tag{III-12}$$

with:

T_{em}: electromagnetic torque.

T_r: resistant torque that can be a function of speed.

J: moment of inertia of the rotating masses.

f: viscous friction coefficient.

Ω_r : Speed of rotation of the machine.

III.3 Park's Transformation

To derive a system of equations with constant coefficients, the stator and rotor windings are transformed into an equivalent set of orthogonal windings. Consequently, the balanced three-phase machine is represented by an equivalent two-phase model defined along the direct (d) and quadrature (q) axes, as illustrated in Fig. (III.2).

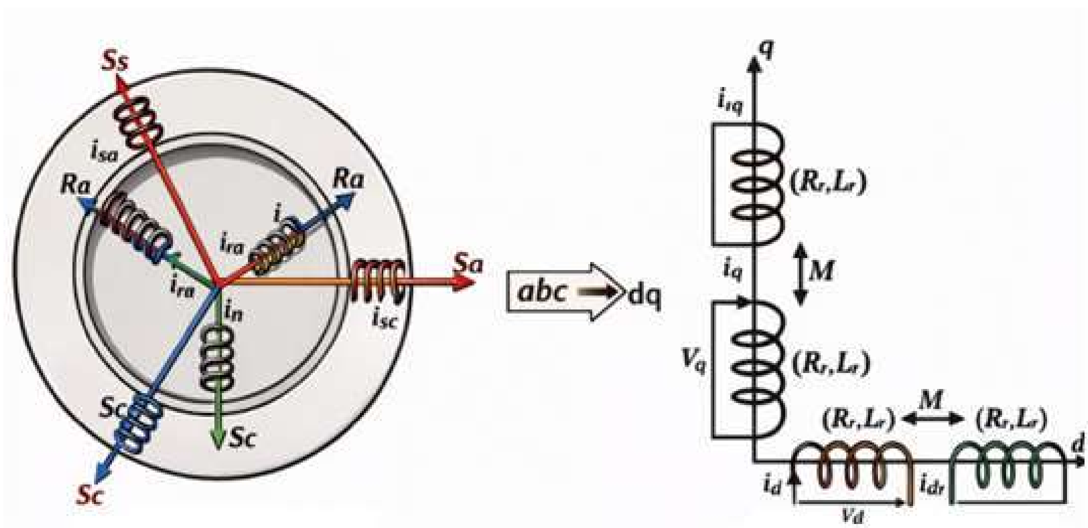

Fig III.2: abc-to-dq reference frame transformation

Within this framework, the d–q reference system significantly simplifies the modeling of electrical machines. By applying the Park transformation, the machine's behavior can be expressed in terms of two equivalent inductances aligned with the d and q axes, rather than three physically distributed phase windings [25]. This transformation facilitates the analysis while relying on a set of simplifying assumptions. The Park transformation's representation, in general, is given as:

$$\left[P(\theta)\right]=\sqrt{\frac{2}{3}}\cdot\begin{bmatrix}\cos(\theta) & \cos\left(\theta-\frac{2\pi}{3}\right) & \cos\left(\theta-\frac{4\pi}{3}\right)\\ -\sin(\theta) & -\sin\left(\theta-\frac{2\pi}{3}\right) & -\sin\left(\theta-\frac{4\pi}{3}\right)\\ \frac{1}{\sqrt{2}} & \frac{1}{\sqrt{2}} & \frac{1}{\sqrt{2}}\end{bmatrix} \quad \text{(III-13)}$$

$$\begin{bmatrix} x_d \\ x_q \\ x_0 \end{bmatrix} = P(\theta) \cdot \begin{bmatrix} x_a \\ x_b \\ x_c \end{bmatrix} \qquad \text{(III-14)}$$

III.3.1 Application of the Park Transformation

The equations of the machine in (III-1) can be reformulated using the transformation matrix, under the assumption that the system is balanced.

III.3.1.1 Electrical Equations

$$\begin{cases} V_{sd} = R_s i_{sd} + \frac{d}{dt}\Phi_{sd} - \omega_a \Phi_{sq} \\ V_{sq} = R_s i_{sq} + \frac{d}{dt}\Phi_{sq} + \omega_a \Phi_{sd} \\ V_{rd} = 0 = R_r i_{rd} + \frac{d}{dt}\Phi_{rd} - (\omega_a - \omega_r)\Phi_{rq} \\ V_{rq} = 0 = R_r i_{rq} + \frac{d}{dt}\Phi_{rq} + (\omega_a - \omega_r)\Phi_{rd} \end{cases} \qquad \text{(III-15)}$$

III.3.1.2 Magnetic Equations

$$\begin{cases} \Phi_{sd} = L_s \cdot i_{sd} + M \cdot i_{rd} \\ \Phi_{sq} = L_s \cdot i_{sq} + M \cdot i_{rq} \\ \Phi_{rd} = L_r \cdot i_{rd} + M \cdot i_{sd} \\ \Phi_{rq} = L_r \cdot i_{rq} + M \cdot i_{sq} \end{cases} \qquad \text{(III-16)}$$

$L_s = l_s - m_s$: the cyclic inductance of the stator

$L_r = l_r - m_r$: the cyclic inductance of the rotor.

$M = \frac{3}{2} M_{sr}$: the mutual cyclic inductance between stator and rotor.

III.3.1.3 Mechanical Equations

Applying the Park transformation to the mechanical equation yields the following expression:

$$T_{em} = \frac{3}{2} p \left(\Phi_{rd} i_{sq} - \Phi_{rq} i_{sd} \right) \qquad \text{(III-17)}$$

The equation of motion of the machine is then written:

$$J . \frac{d\Omega_r}{dt} = T_{em} - T_r - f . \Omega_r \qquad \text{(III-18)}$$

III.4 Model of the Induction Motor

To formulate the machine model in a state-space representation, the governing equations must be reformulated in terms of the state vector X_u. After appropriate simplification and rearrangement, the system can be expressed in the following form [26]:

$$\dot{X}_u = A_u \cdot X_u + B_u U \tag{III-19}$$

With:

$$A=\begin{bmatrix} 0 & \omega_{dq} & -R_s & 0 \\ -\omega_{dq} & 0 & 0 & -R_s \\ \dfrac{1}{\sigma L s T_r} & \dfrac{1}{\sigma L_s}\omega_r & -\dfrac{1}{\sigma T_s}-\dfrac{1}{\sigma T_r} & \omega_{dq}-\omega_r \\ -\dfrac{1}{\sigma L_s}\omega_r & \dfrac{1}{\sigma L_s T_r} & -(\omega_{dq}-\omega_r) & -\dfrac{1}{\sigma T_s}-\dfrac{1}{\sigma T_r} \end{bmatrix} ; \quad B=\begin{bmatrix} 1 & 0 \\ 0 & 1 \\ \dfrac{1}{\sigma L_s} & 0 \\ 0 & \dfrac{1}{\sigma L_s} \end{bmatrix} \quad U=\begin{bmatrix} V_{ds} \\ V_{qs} \end{bmatrix}$$

and: $T_r = \dfrac{L_r}{R_r}$; $\delta = 1 - \dfrac{M^2}{\delta L_s L_r}$; $T_s = \dfrac{L_s}{R_s}$.

The system variables were transformed from the d–q reference frame to the α–β reference frame.

III.5 Simulation of the Induction Motor

Fig.III.3 illustrates the block diagram of the induction motor simulation implemented in MATLAB/Simulink. In this model, the motor is directly supplied by a three-phase electrical network with a line voltage of 220/380 V at a frequency of 50 Hz. The detailed parameters used for the induction motor model are provided in the Appendix x.

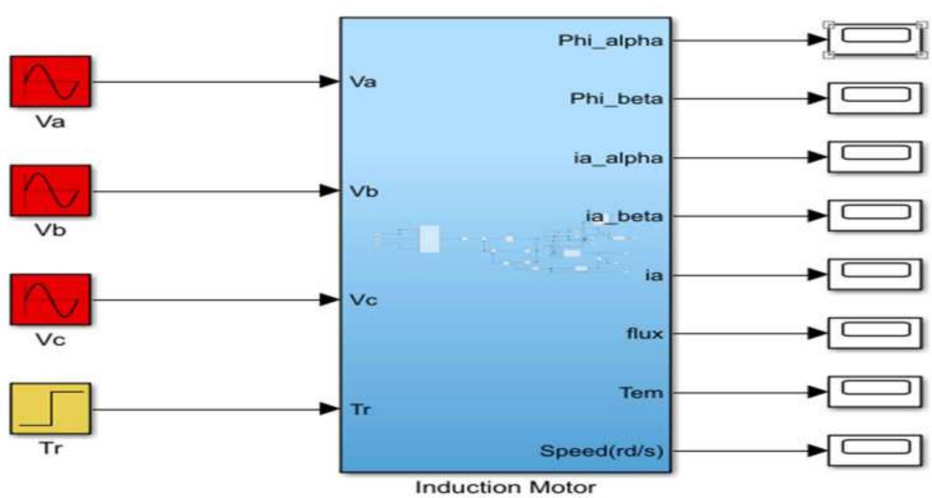

Fig III.3: Block diagram of induction motor simulation.

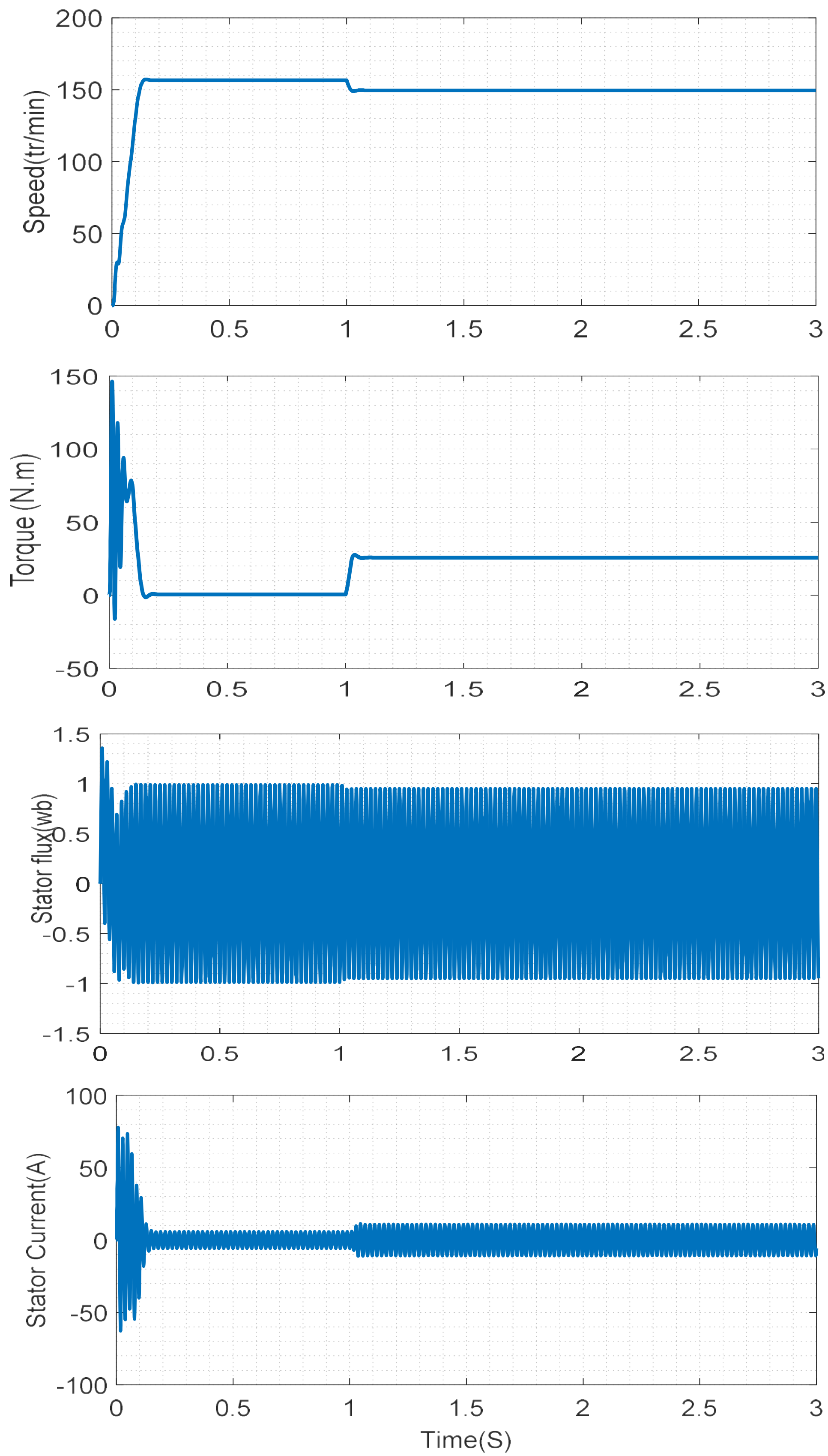

Fig III.4: Simulation of the induction motor for (T_r=25.5 Nm, t = 1 s)

Fig. III.4 illustrates the dynamic and steady-state behavior of a three-phase induction motor. At startup, a high inrush stator current is observed due to the absence of back electromotive force, followed by a gradual stabilization. The rotor speed increases rapidly and reaches near its nominal value, indicating a fast transient response. Around t≈1s, the application of a mechanical load causes a slight drop in speed, accompanied by an increase in stator current and electromagnetic torque, reflecting the system's adaptation to the new operating condition. The electromagnetic torque initially exhibits high oscillations to accelerate the rotor, then stabilizes, and rises again under load. Meanwhile, the stator flux remains relatively constant after the transient phase, confirming that it is mainly governed by the supply voltage. Overall, the results demonstrate a stable and realistic performance of the induction motor under both no-load and load conditions.

III.6 Modeling of the Centrifugal Pump

The mathematical modeling of the centrifugal pump is essential for accurately describing its hydraulic and mechanical behavior within the studied system. The relationship between the flow rate and the generated head can be represented using the *Pfleider–Peterman* quadratic model, where the rotational speed is introduced as a parameter [27]. This relationship is expressed as follows:

$$H = a_0\omega^2 + a_1\omega\varphi + a_2\varphi^2 \qquad \text{(III-20)}$$

With:

φ: The water flow (m^3/s)

H: The total height (m)

ω: Rotation speed (rad/s)

a_0, a_1, a_2: are the coefficients given by the manufacturers.

The Q–H characteristic of the pipe network can be expressed by:

$$H = H_g + \psi\ \varphi^2 \qquad \text{(III-21)}$$

ψ: is a constant which depends on conduit diameter and on all frictional losses of the pipe network.

H_g: is the geodesic height (m).

From a mechanical perspective, the centrifugal pump exerts a load torque on the driving motor that is proportional to the square of the rotational speed. This relationship can be written as:

$$T = k_{pump} \cdot \omega^2 \qquad \text{(III-22)}$$

k_{pump}: denotes the proportionality coefficient.

Finally, the performance of the centrifugal pump at different operating speeds can be derived using the affinity (similarity) laws. These laws establish proportional relationships between flow rate, head, and power for varying rotational speeds, and are expressed as follows:

$$\varphi' = \varphi \frac{\omega'}{\omega} \quad \text{(III-23)}$$

These equations are fundamental for predicting pump performance under variable speed conditions and are widely used in simulation and control of pumping systems.

III.7 Modeling the Voltage Source Inverter (VSI)

The switching states of the inverter, assumed to be ideal, are represented by three Boolean control variables S_i with i=a, b, c. Each variable defines the conduction state of the corresponding inverter leg. When the upper switch of a leg is conducting, $S_i=1$ conversely, when the lower switch is conducting $S_i=0$.

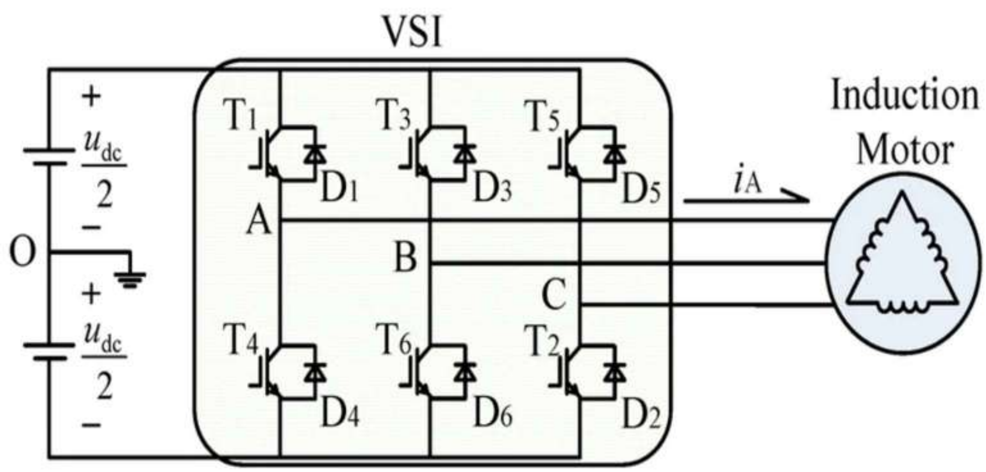

Fig III.5: Three-phase VSI fed star-connected induction machine.

Based on these switching states, the phase (simple) voltages applied to the three stator windings are determined with respect to the fictitious neutral point o. The corresponding expressions can be derived as follows [28].

$$\begin{cases} V_{an} = V_{ao} + V_{on} \\ V_{bn} = V_{bo} + V_{on} \\ V_{cn} = V_{co} + V_{on} \end{cases} \quad \text{(III-24)}$$

By addition on a:

$$V_{an} + V_{bn} + V_{cn} = V_{ao} + V_{bo} + V_{co} + 3\,V_{on} \quad \text{(III-25)}$$

Since the three-phase stator voltage system is symmetrical, the following relation holds:

$$V_{ao} + V_{bo} + V_{co} + 3\,V_{on} = 0 \quad \text{(III-26)}$$

Consequently, the following result emerges:

$$V_{on} = \frac{1}{3}(V_{ao} + V_{bo} + V_{co}) \tag{III-27}$$

By substituting (III-30) into the system of equations (III-27), the resulting expressions can be obtained as follows:

$$\begin{cases} V_{an} = \frac{1}{3}(2\,V_{ao} - V_{bo} - V_{co}) \\ V_{bn} = \frac{1}{3}(-V_{ao} + 2\,V_{bo} - V_{co}) \\ V_{cn} = \frac{1}{3}(-V_{ao} - V_{bo} + 2\,V_{co}) \end{cases} \tag{III-28}$$

After rearranging the equations of both systems, the resulting matrix form can be expressed as follows:

$$\begin{bmatrix} V_{an} \\ V_{bn} \\ V_{cn} \end{bmatrix} = \frac{1}{3} \cdot \begin{bmatrix} 2 & -1 & -1 \\ -1 & 2 & -1 \\ -1 & -1 & 2 \end{bmatrix} \cdot \begin{bmatrix} V_{ao} \\ V_{bo} \\ V_{co} \end{bmatrix} \tag{III-29}$$

with:

$$\begin{aligned} V_{ao} &= E.S_a \\ V_{bo} &= E.S_b \\ V_{co} &= E.S_c \end{aligned} \tag{III-30}$$

Finally, there exists:

$$\begin{bmatrix} V_{an} \\ V_{bn} \\ V_{cn} \end{bmatrix} = \frac{E}{3} \cdot \begin{bmatrix} 2 & -1 & -1 \\ -1 & 2 & -1 \\ -1 & -1 & 2 \end{bmatrix} \cdot \begin{bmatrix} S_a \\ S_b \\ S_c \end{bmatrix} \tag{III-31}$$

III.7.1 Sinusoidal PWM control strategy

To determine the switching instants of the power devices, the Pulse Width Modulation (PWM) technique is employed. In particular, the sinusoidal PWM (SPWM) method is adopted, which is based on comparing three sinusoidal reference signals, known as modulating voltages, with a high-frequency triangular waveform referred to as the carrier signal. The intersection between the modulating signals and the carrier waveform defines the switching states of the inverter. The reference voltages are expressed as follows: The implementation of the sinusoidal PWM control in simulation is depicted in Fig. (II.8).

$$\begin{cases} V_{sa_{ref}}(t) = r \cdot \frac{V_{dc}}{2} \sin(\omega_r t) \\ V_{sb_{ref}}(t) = r \cdot \frac{V_{dc}}{2} \sin(\omega_r t - \frac{2\pi}{3}) \\ V_{sc_{ref}}(t) = r \cdot \frac{V_{dc}}{2} \sin(\omega_r t + \frac{2\pi}{3}) \end{cases} \quad \text{(III-32)}$$

with: $\omega_r = 2\pi f_r$

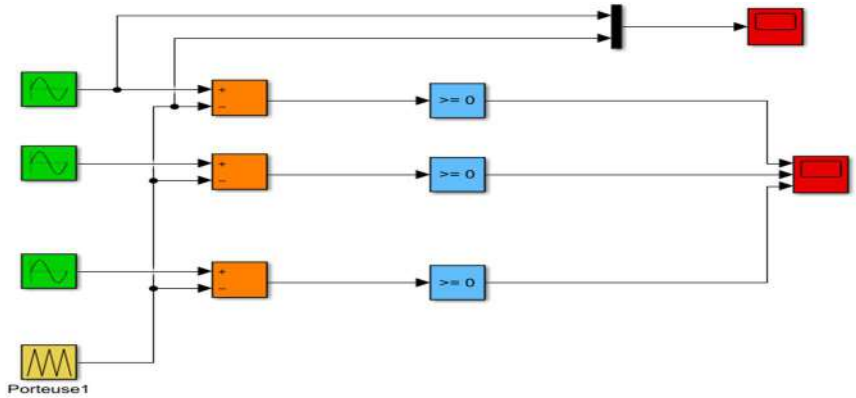

Fig III.6: Simulation diagram of the sinusoidal PWM control

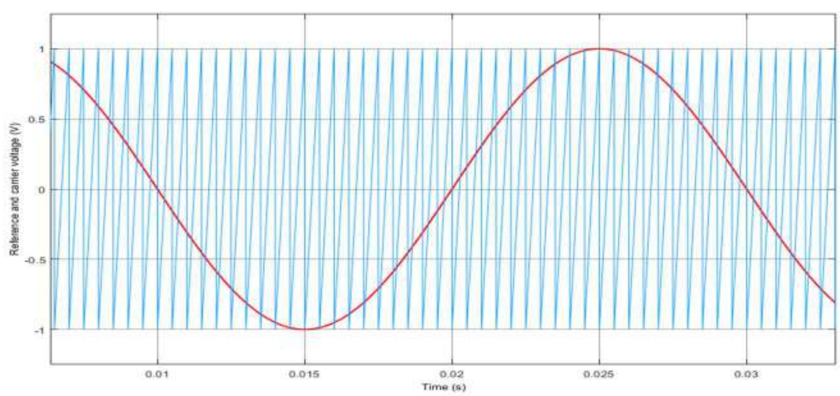

Fig III.7: Representation of the carrier and the modulator

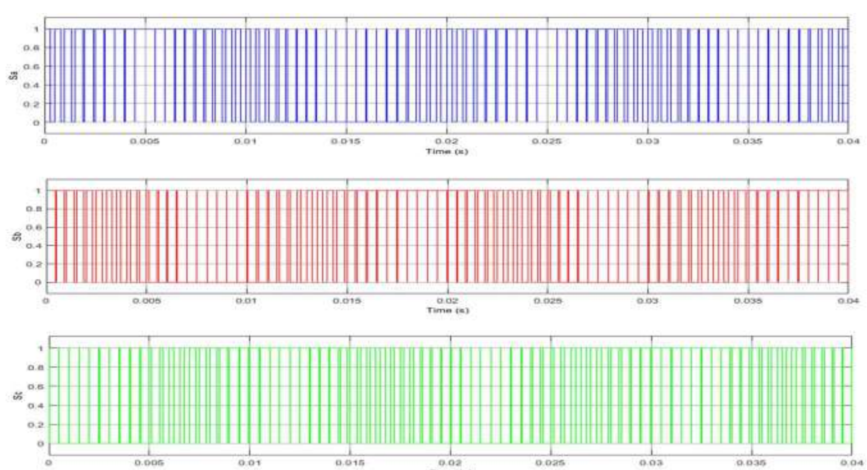

Fig III.8: Results of simulation of control signals.

Two parameters characterize the control strategy. The first is the modulation index mmm, which is defined as the ratio of the amplitude of the reference signal to that of the carrier signal:

$$m = \frac{f_p}{f_{ref}} \tag{III-33}$$

The voltage adjustment coefficient r is defined as the ratio of the amplitude of the reference voltage to the peak value of the carrier signal.

$$r = \frac{V_{ref}}{V_p} \tag{III-34}$$

III.7 Simulation of the IM with inverter

The Fig.III.9 illustrates the overall control and simulation scheme of a three-phase voltage source inverter (VSI) fed induction motor. The results presented in Fig. III.10 show that the stator flux remains nearly sinusoidal with a constant amplitude after a short transient period, confirming stable magnetic operation of the machine. The stator current exhibits a high inrush at startup, followed by damped oscillations before settling into a steady periodic regime influenced by PWM switching effects. The electromagnetic torque presents significant oscillations during the starting phase, then stabilizes at a lower steady-state value, with a noticeable increase at t = 1 s corresponding to the application of load. The rotor speed increases rapidly toward its steady-state value, with a slight transient drop at the instant of load disturbance, which highlights the good dynamic response and overall stability of the system.

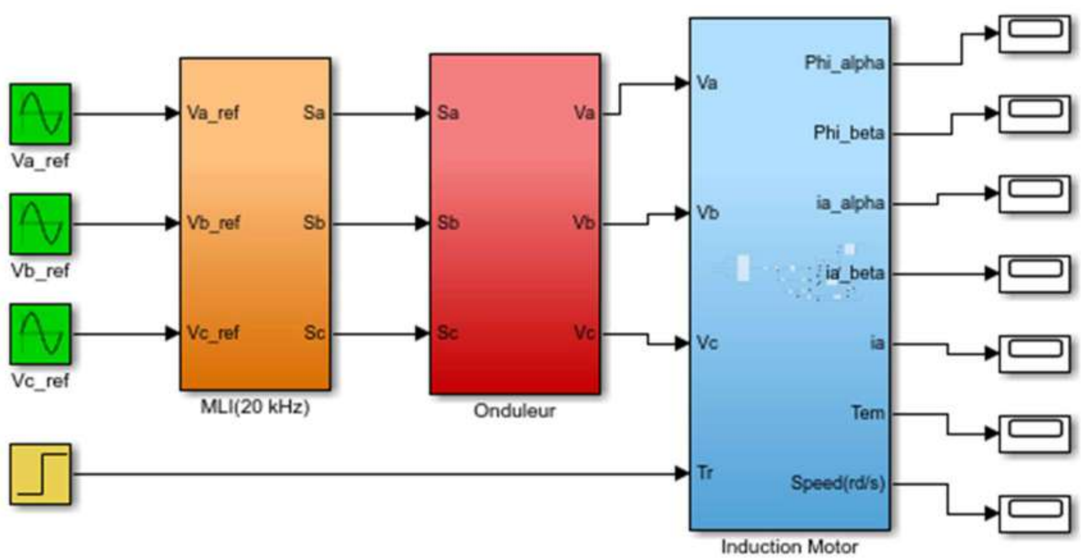

Fig. III.9: Control structure of the VSI-fed induction motor drive

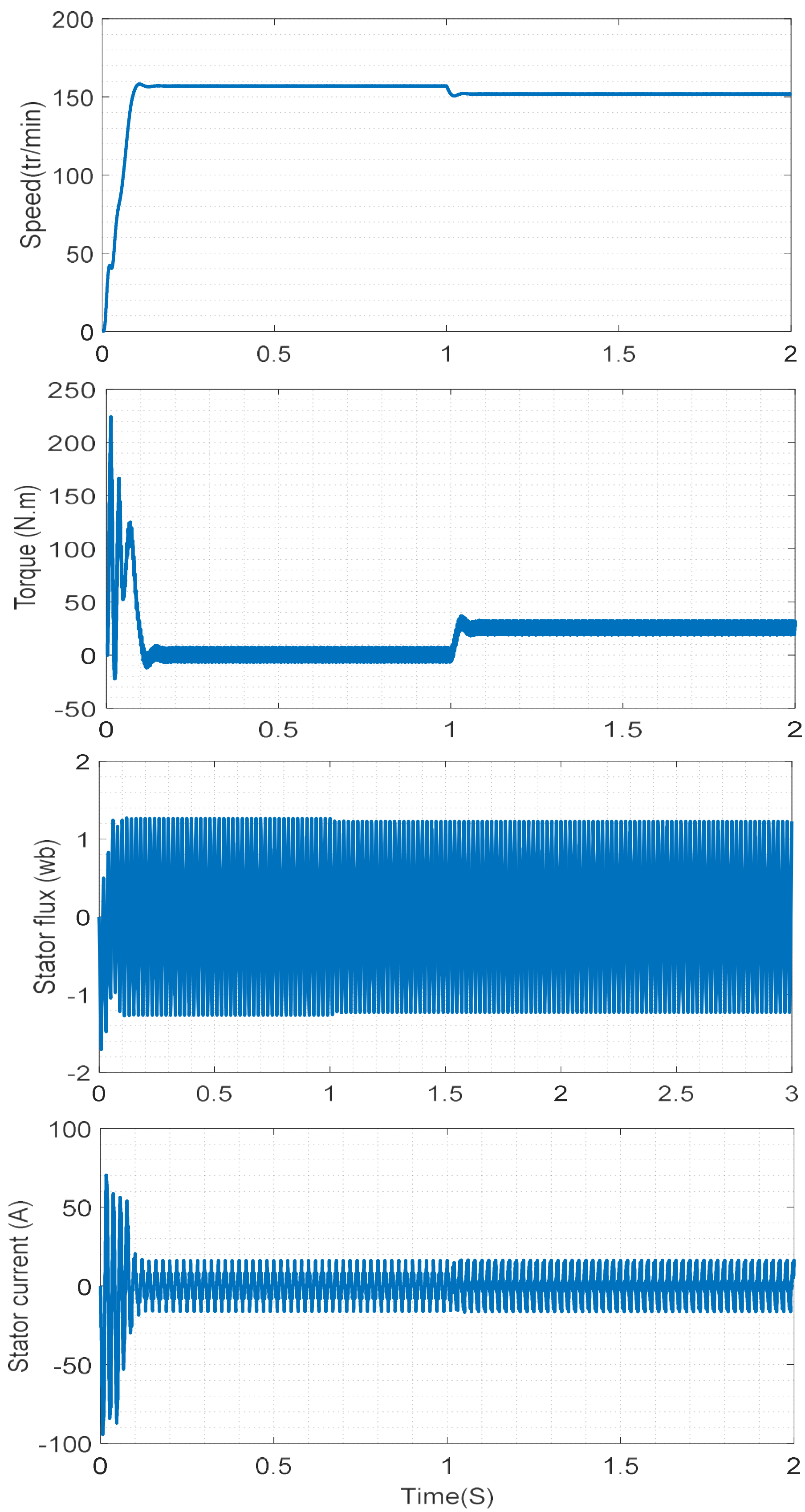

Fig III.10: Simulation of the IM with inverter for (T_r=25.5 Nm, t = 1 s)

III.8 Conclusion

This chapter presented the mathematical modeling of the main components of a solar photovoltaic water pumping system, namely the induction motor, the centrifugal pump, and the voltage source inverter. The induction motor model was developed in the α–β reference frame, which allows an accurate dynamic representation of the electrical and mechanical interactions, and facilitates its integration within control and simulation frameworks. Furthermore, a detailed mathematical model of the centrifugal pump was established to describe the relationship between its hydraulic variables flow rate, head, and efficiency and its mechanical operating conditions, particularly the rotational speed and developed torque. This model is essential for accurately capturing the nonlinear behavior of the pumping subsystem under varying operating conditions.

Finally, the inverter was modeled as a controlled power electronic interface responsible for converting the DC power generated by the photovoltaic array and regulated by the boost converter into an AC voltage with variable magnitude and frequency suitable for driving the induction motor. This stage plays a key role in ensuring proper energy transfer and dynamic control of the overall system.

Chapter IV.

PI-GTO-Based Direct Torque Control for Photovoltaic Water Pumping Systems

IV.1 Introduction

Direct Torque Control (DTC) is one of the most widely used control techniques for induction motor drives due to its simple structure, fast dynamic response, and effective torque control capability. However, conventional DTC suffers from several drawbacks, such as torque ripples, flux oscillations, and sensitivity to parameter variations, which may affect the overall performance of the photovoltaic water pumping system. To improve the dynamic and steady-state performance of the control system, this chapter proposes the use of a Proportional-Integral (PI) controller optimized by the Gorilla Troops Optimizer (GTO) algorithm. The GTO algorithm is a recent metaheuristic optimization technique inspired by the social behavior and movement strategies of gorilla troops in nature. It is employed to determine the optimal PI controller parameters in order to enhance speed regulation, reduce torque ripples, and improve system stability.

This chapter presents the operating principle of the DTC strategy, the design of the PI controller, and the implementation of the GTO optimization algorithm. Finally, simulation results are discussed to evaluate the effectiveness and robustness of the proposed control approach under different operating conditions.

IV.2. DTC for Photovoltaic Water Pumping System

Photovoltaic Water Pumping Systems (PVWPS) are widely used as sustainable and autonomous solutions for water supply in remote and agricultural areas. A typical PWPS consists of a photovoltaic generator, a power electronic converter with MPPT, an electric motor drive, and a centrifugal pump. To improve the performance of the motor drive, DTC is commonly employed due to its simple structure, fast dynamic response, and robust operation under varying solar irradiance conditions. DTC directly controls the electromagnetic torque and stator flux through appropriate inverter switching states, ensuring efficient and reliable operation of the water pumping system.

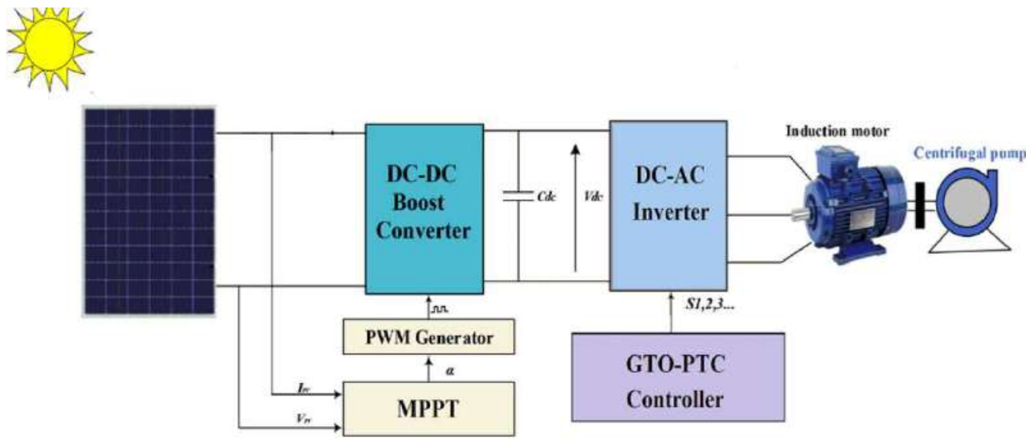

Fig. IV.1: Overall configuration of the DTC-based PVWPS

IV.2.1 Principle of DTC

DTC is a high-performance strategy for AC motor drives characterized by a simple structure and fast dynamic response. It directly regulates stator flux and electromagnetic torque without inner current loops or complex coordinate transformations, unlike Field-Oriented Control. In DTC, stator flux and torque are estimated from measured stator voltages and currents, then compared with their references using hysteresis controllers. Based on the resulting errors, an optimal inverter voltage vector is selected from a predefined switching table in the stationary (α, β) frame according to the flux position and required torque/flux variations. Unlike PWM-based methods, DTC directly determines inverter switching states, enabling rapid torque response, reduced computational effort, and robust performance under parameter variations and load disturbances. These advantages make it well suited for applications such as photovoltaic water pumping systems, where fast adaptation to changing conditions is essential [29].

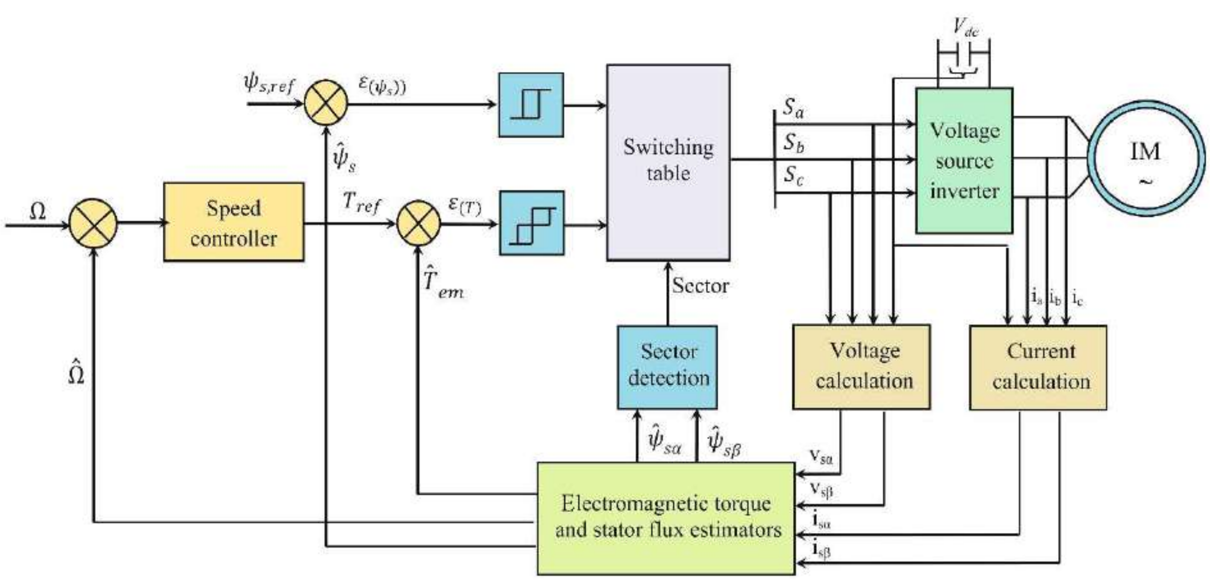

Fig.IV.2: Block diagram of DTC-IM

IV.2.3 Stator Flux and Electromagnetic Torque Estimation

In DTC, stator flux and electromagnetic torque are not directly measured but estimated from stator voltages and currents in the (α, β) frame. The flux is obtained through voltage integration, while the torque is computed from the interaction between flux and current vectors. These estimations enable real-time control and accurate inverter switching decisions [30].

In the (α-β) reference frame, the stator voltage can be calculated based on the bus voltage V_{dc} and the switches (S_a, S_b, S_c) as follows:

$$\begin{cases} V_{\alpha s} = \sqrt{\frac{3}{2}} V_{dc}(S_a - \frac{1}{2}(S_b + S_c)) \\ V_{\beta s} = \sqrt{\frac{1}{2}} V_{dc}(S_b - S_c) \end{cases} \tag{IV-1}$$

The stator current components ($i_{\alpha s}$, $i_{\beta s}$) are expressed by applying the Concordia transformation to the three-phase components I_{sa}, I_{sb}, and I_{sc} as follows:

$$\begin{cases} i_{\alpha s} = \sqrt{\frac{3}{2}} I_{sa} \\ i_{\beta s} = \frac{1}{\sqrt{2}} (I_{sa} - I_{sb}) \end{cases} \tag{IV-2}$$

IV.2.3.1 Stator Flux Estimation

The stator flux vector in the stationary (α, β) reference frame is defined as:

$$\vec{\psi}_s = \int (\vec{v}_s - R_s \vec{i}_s) dt \tag{IV-3}$$

The magnitude of the stator flux vector is determined from its two-phase components:

$$\psi_s = \sqrt{\psi_\alpha^2 + \psi_\beta^2} \tag{IV-4}$$

In the stationary (α–β) reference frame, the stator flux components are expressed as follows:

$$\begin{cases} \psi_{\alpha s} = \int (V_{\alpha s} - R_s i_{\alpha s}) dt \\ \psi_{\beta s} = \int (V_{\beta s} - R_s i_{\beta s}) dt \end{cases} \tag{IV-5}$$

The position of stator flux angle is obtained by Eq. (IV.6):

$$\theta_s = \tan^{-1}\left(\frac{\psi_\beta}{\psi_\alpha}\right) \tag{IV-6}$$

IV.2.3.2 Electromagnetic Torque Estimation

The electromagnetic torque is estimated from the stator flux components and the measured current components according to the following expression:

$$T_e = \frac{3}{2} p(\psi_\alpha i_\beta - \psi_\beta i_\alpha) \tag{IV-7}$$

IV.2.4 Hysteresis Controllers in DTC

Hysteresis controllers are essential components in DTC, ensuring that the stator flux and electromagnetic torque remain within predefined tolerance bands around their reference values. Based on the instantaneous control errors, these controllers generate discrete signals used by the switching table to select the appropriate inverter voltage vector. Their simple structure and fast response contribute significantly to the high dynamic performance of DTC systems.

IV.2.4.1 Flux Corrector

The flux hysteresis controller maintains the stator flux vector within a predefined circular hysteresis band, as illustrated in Fig. (IV.3). Its output, represented by the Boolean variable C_{flx}, indicates whether the flux magnitude must be increased (C_{flx}=1) or decreased (C_{flx}=0) to keep the stator flux within the specified limits.

$$\left|\psi_{ref} - \psi_s\right| \leq \Delta\psi_s \qquad \text{(IV-8)}$$

With:

ψ_{ref}: The reference flux.

$\Delta\psi_s$: the hysteresis width of the corrector.

Subsequently, the expression can be formulated as follows:

$$\begin{cases} si\ \Delta\psi_s > \mathcal{E}_\psi \\ si\ 0 \leq \Delta\psi_s \leq \mathcal{E}_\psi \\ si\ 0 \leq \Delta\psi_s \leq \mathcal{E}_\psi \\ si\ \Delta\psi_s < -\mathcal{E}_\psi \end{cases} \text{and} \begin{cases} d\Delta\psi_s/dt > 0 \\ d\Delta\psi_s/dt < 0 \end{cases} \dots\dots \begin{cases} \text{So } C_{flx} = 1 \\ \text{So } C_{flx} = 0 \\ \text{So } C_{flx} = 1 \\ \text{So } C_{flx} = 0 \end{cases} \qquad \text{(IV-9)}$$

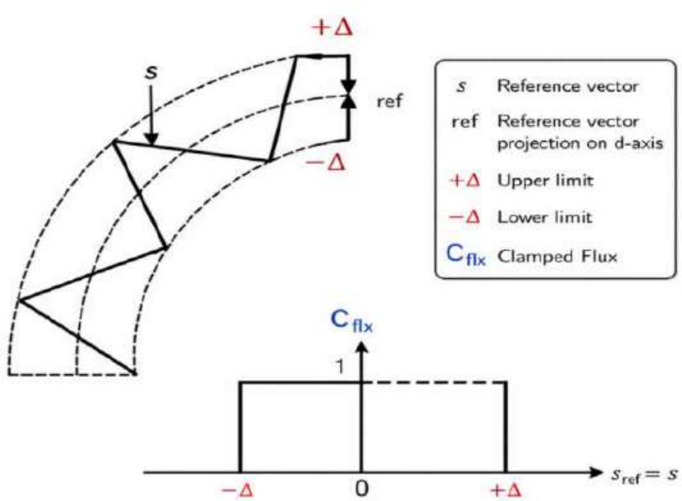

Fig IV.3: Principle of stator flux hysteresis control

Fig.IV.3 presents the operation of the flux hysteresis controller, where the flux magnitude is constrained between the upper (+Δ) and lower (−Δ) hysteresis limits around the reference value. The controller output C_{flx} determines whether the flux should be increased or decreased to maintain stable flux regulation and ensure fast dynamic response [31].

IV.2.4.2 Torque Corrector

The purpose of the torque corrector is to maintain the torque within the permissible limits defined as follows [32], (Fig.IV.4. a):

$$\left|T_{ref} - T_e\right| \leq \Delta T_e \quad \text{(IV-10)}$$

With:

T_{ref} : The reference torque,

ΔT_e : The hysteresis band of the corrector.

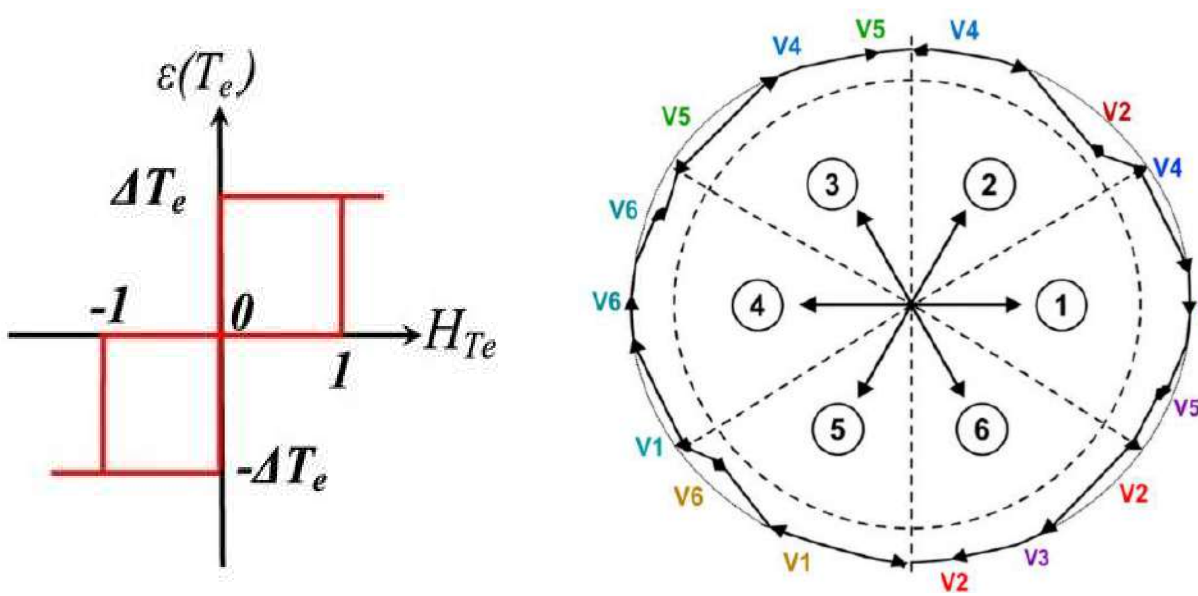

(a) (b)

Fig. IV.4: (a) Electromagnetic torque hysteresis comparator and (b) selection of voltage vectors

IV.2.5 Switching Table and Selection of Voltage Vectors

Fig. IV.4.b illustrates the trajectory of the stator flux vector within a circular hysteresis band in the stationary (α, β) reference frame. The appropriate voltage vectors V_1−V_6 are selected to maintain the stator flux within the prescribed hysteresis limits and achieve the desired flux variation. Based on the outputs of the flux and torque hysteresis controllers and the position of the stator flux vector, the switching table (Table IV.1) selects the appropriate inverter voltage vector. The stator flux plane is divided into six sectors, where each sector corresponds to predefined switching states designed to increase or decrease the stator flux and electromagnetic torque as required. This strategy ensures fast dynamic response without the need for PWM modulation [33].

Table IV.1: Switching table for voltage vector selection in DTC

N		1	2	3	4	5	6	COMPARATOR
$C_{flx}=1$	$C_{trq}=1$	V_2	V_3	V_4	V_5	V_6	V_1	2 LEVELS
	$C_{trq}=0$	V_7	V_0	V_7	V_0	V_7	V_0	
	$C_{trq}=-1$	V_6	V_1	V_2	V_3	V_4	V_5	3 LEVELS
$C_{flx}=0$	$C_{trq}=1$	V_3	V_4	V_5	V_6	V_1	V_2	2 LEVELS
	$C_{trq}=0$	V_0	V_7	V_0	V_7	V_0	V_7	
	$C_{trq}=-1$	V_5	V_6	V_1	V_2	V_3	V_4	3 LEVELS

IV.3 PI Controller Design for DTC

In DTC, the PI controller regulates speed by minimizing the error between reference and measured values, improving system stability and dynamic response. However, conventional fixed gains (K_p, K_i) suffer from limited robustness under nonlinearities, parameter variations, and disturbances, (Fig IV.5). This motivates the use of optimization methods such as the Gorilla Troops Optimizer (GTO) for optimal PI tuning and enhanced performance.

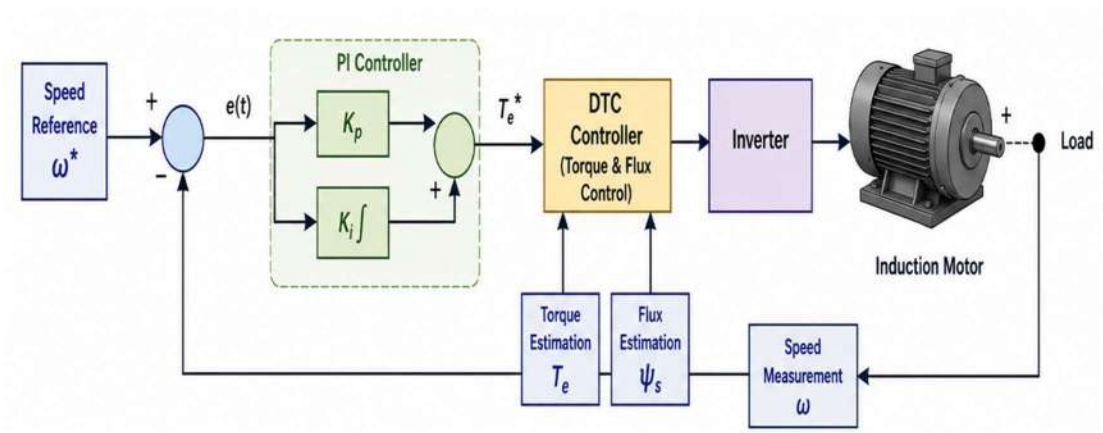

Fig IV.5: Structure of the PI-based speed control loop in DTC

IV.4 Gorilla Troops Optimizer

The GTO is a nature-inspired metaheuristic algorithm derived from the social hierarchy and cooperative behavior of wild gorillas. The optimization process is guided by the dominant silverback, representing the best candidate solution, while the remaining gorillas contribute to the exploration of the search space. The GTO algorithm mainly operates through two complementary phases, (Fig IV.6): exploration and exploitation, which are described below[34].

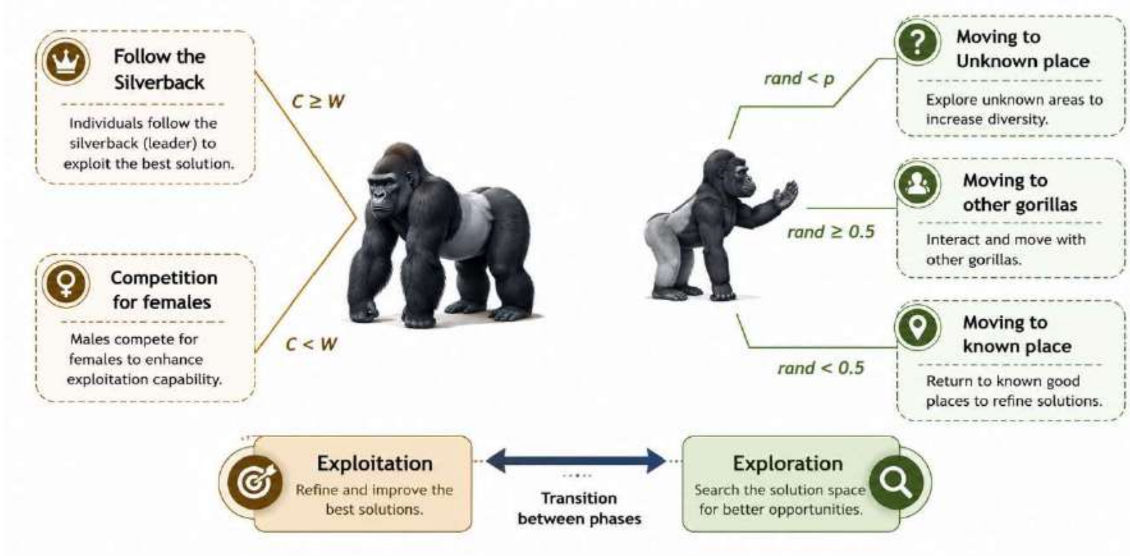

Fig IV.6: Main exploration and exploitation phases of the GTO algorithm

A. Exploration Phase (Global Search)

In this phase, every gorilla denotes a potential solution, whereas the silverback gorilla signifies the optimal solution. The exploration of the search space is governed by three distinct behavioral strategies that regulate the updating of gorilla positions as defined in Eq. (IV-11).

1. Migration toward former locations.
2. Migration into completely unexplored areas.
3. Movement to alternative troops.

$$GY(t+1)=\begin{cases}(U_B-L_B)\times r_1+L_B\,, & r<P\\ (r_2-C)\times Y_R(t)+Q\times D, & r\geq 0.5\\ Y(t)-Q\times(Q+r_3)\times(Y(t)-GY_R(t)), & r<0.5\end{cases} \quad \text{(IV-11)}$$

and

$$C=(C\,os(\,2.r_4)+1).\left(1-\frac{t_i}{T_{iter}}\right) \quad \text{(IV-12)}$$

where:

$GY(t+1)$: represents the position vector of the gorilla for the subsequent iteration.

U_B and L_B: indicate the limit bounds of the variables.

r_1, r_2, r_3, and r are random values in [0, 1].

$Y(t)$: It is the gorilla's current position vector.

$Y_R(t)$ and $GY_R(t)$ are the candidate position vectors of gorillas that are selected randomly.

r_4: a random number [–1, 1],

T_{iter}: is the maximum number of iterations.

C, Q, D: adaptive parameters, and P is a constant parameter.

The value of L is expressed as follows:

$$L = C \times v \tag{IV-13}$$

v is a random value [–1, 1], H: Vector calculated as:

$$H = Z \times Y(t), \text{ and } Z = [-C, C] \tag{IV-14}$$

B. Exploitation Phase (Local Refinement)

The GTO algorithm adopts two principal behavioral strategies:

1. Tracking the silverback,
2. Competing for adult females.

A transition mechanism between the two strategies is based on comparing the coefficient C (Eq. IV-12) with a threshold value V defined at initialization. This transition is expressed in Eq. (IV-15):

$$GY(t+1) = L \times W \times (Y(t) - Y_{silverback}) + Y(t) \tag{IV-15}$$

where: $Y_{Silverback}$ represents the optimal solution identified. W can be calculated as follows:

$$W = \left(\left|\frac{1}{n}\sum_{i=1}^{n} GY_i(t)\right|^{2^L}\right)^{\frac{1}{2^L}} \tag{IV-16}$$

n refers to the population size.

When $C < V$, the latter mechanism is selected, and the gorilla positions are updated as follows:

$$GY(i) = Y_{silverback} - A \times (Y_{silverback} \times Q - Y(t) \times K) \tag{IV-17}$$

$$Q = (2 \times r_5 - 1) \tag{IV-18}$$

$$A = \varphi \times E \tag{IV-19}$$

$$E = \begin{cases} N_1, & r \geq 0.5 \\ N_2, & r < 0.5 \end{cases} \tag{IV-20}$$

and

Q: Simulate the impact effect.

r_5: a random value in [0, 1].

A: It expresses the intensity of the competition.

φ: control the parameter must be predefined at the beginning.

E: used to simulate the influence of violence on the solution dimensions.

r: random value in [0, 1].

IV.4.1 GTO-Based PI Parameter Optimization

In this context, the GTO is employed to optimally tune the proportional-integral (PI) controller parameters by minimizing a predefined objective function related to tracking error and system performance, (Fig.IV.7). This optimization approach enhances dynamic response, improves robustness, and overcomes the limitations associated with conventional tuning methods.

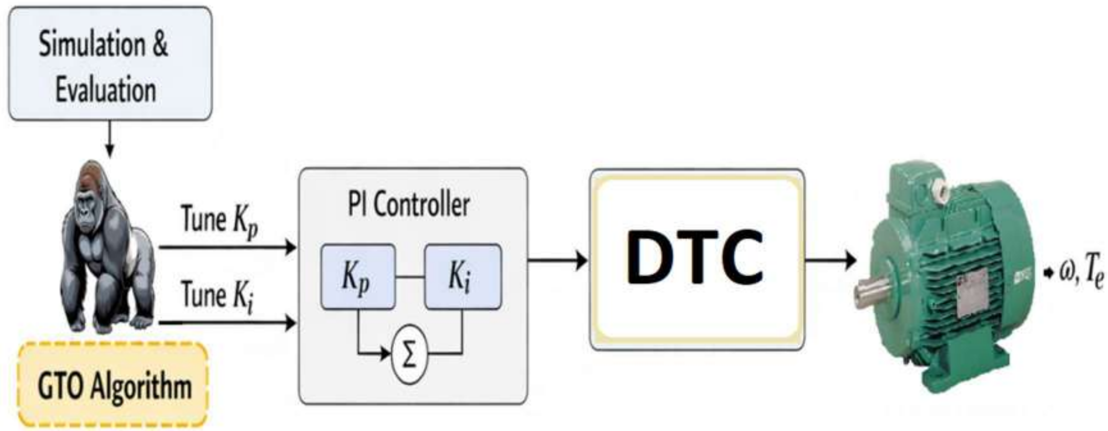

Fig.IV.7: PI-GTO for DTC

IV.4.2 Objective Function

The PI controller gains K_p and K_i are optimized using the GTO algorithm. The objective function J is defined to minimize the integral of time-weighted absolute error of the rotor speed and the torque ripple:

$$J(K_p, K_i) = \omega_1 \int_0^T |\omega_{ref}(t) - \omega(t)|dt + (1 - \omega_1) \int_0^T |T_{ref}(t) - T_e(t)|dt \quad \text{(IV-21)}$$

where ω_{ref} and ω denote the reference and actual rotor speeds, respectively, while T_{ref} and T_e represent the reference and actual torque values over the evaluation interval T. The weighting coefficient ω_1 allows balancing the relative importance of dynamic performance and torque ripple reduction.

The optimization is subject to the inequality constraints defined in Eq. (IV-22), which limit the PI controller gains within predefined lower and upper bounds to ensure system stability.

$$\begin{cases} K_p^{min} \le K_p \le K_p^{max} \\ K_i^{min} \le K_i \le K_i^{max} \end{cases} \quad \text{(IV-22)}$$

This formulation ensures that the GTO algorithm tunes the PI gains to achieve fast reference-speed tracking while minimizing torque and flux ripples, balancing dynamic performance and stability.

Fig. IV.8 illustrates the proposed GTO-DTC strategy applied to the photovoltaic water pumping system. In this control scheme, the GTO is employed to optimally tune the PI controller gains (K_p, K_i), thereby improving the DTC performance in terms of dynamic response, torque and flux regulation, and robustness under varying operating conditions.

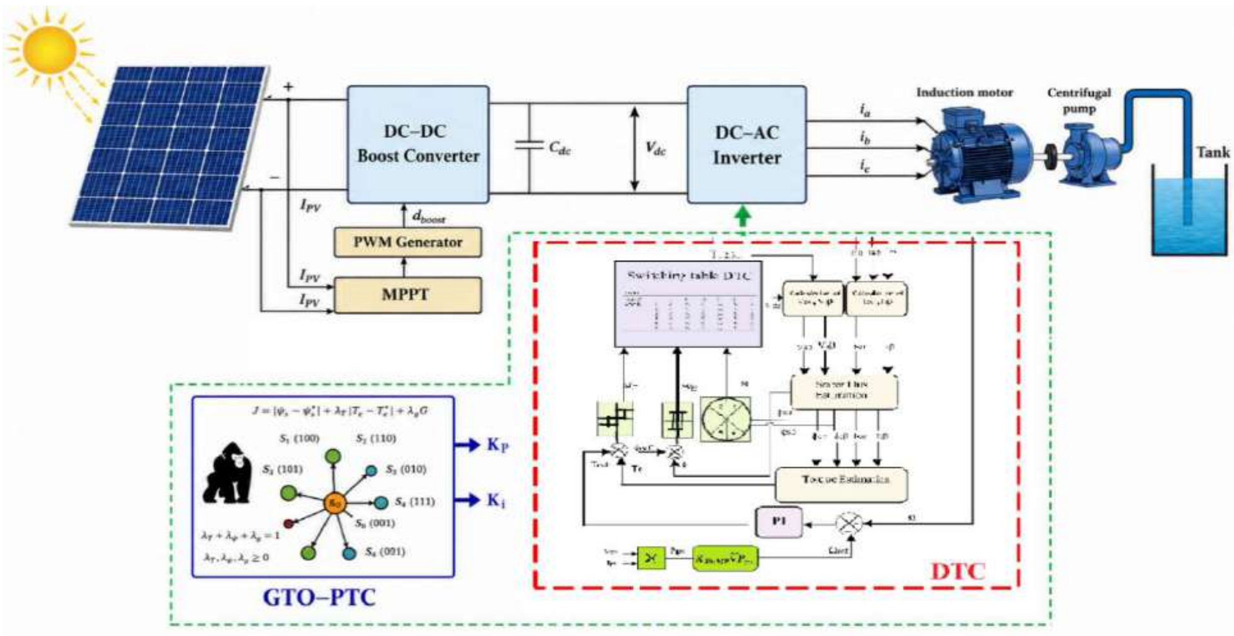

Fig.IV.8: Proposed GTO-based PI-DTC control structure for PVWPS

The main parameters adopted in the GTO algorithm are presented in Table IV.2, whereas the optimized PI controller gains and the corresponding dynamic response characteristics are summarized in Table IV.3 and illustrated in Fig. IV.9.

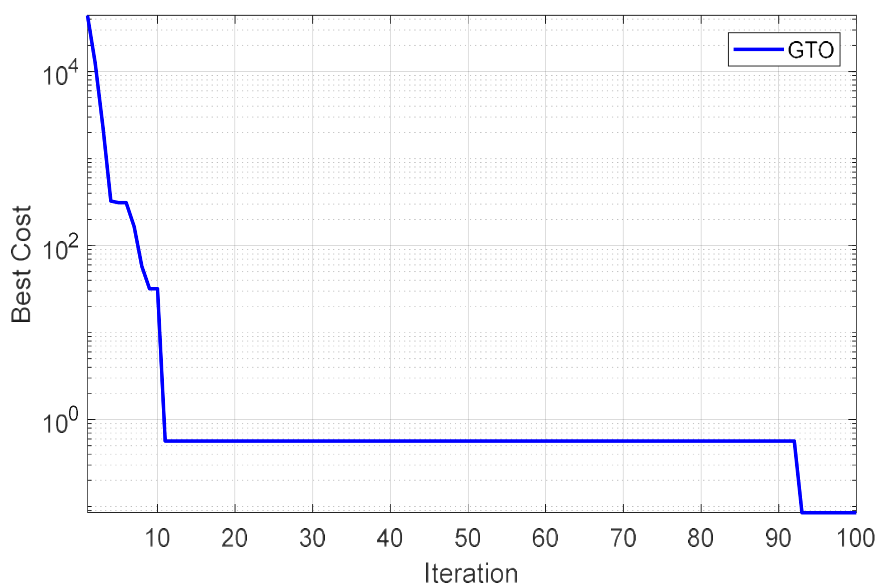

Fig. IV.9: Convergence of GTO algorithm

Table IV.2: Parameters of the GTO algorithm

Description	**Value**
Size of Generation N	40
Iteration limit MaxIter	150
Control parameters λ, β and x	0.04, 3, and 0.7

Table IV.3: Optimal PI gains and dynamic response of tuned controllers

Controller / Loop	K_p	K_i	Peak Time (Tp)	Rise Time (tr)	Settling Time (ts)
PI-DTC	13	0.05	0.32	0.15	0.35
PI-GTO-DTC	55	1.01	0.13	0.04	0.15

IV.5. Simulation Results and Discussion

This section presents a detailed assessment and performance analysis of the PVWPS using MATLAB/Simulink simulations. The study compares different control strategies, namely conventional DTC and PI-GTO-DTC strategy approach. The electrical and mechanical parameters of the photovoltaic array, boost converter, and induction motor are summarized in Tables IV.1, IV.2, and IV.3, respectively.

IV.5.1 Performance DTC under 100 a -100 rad/s

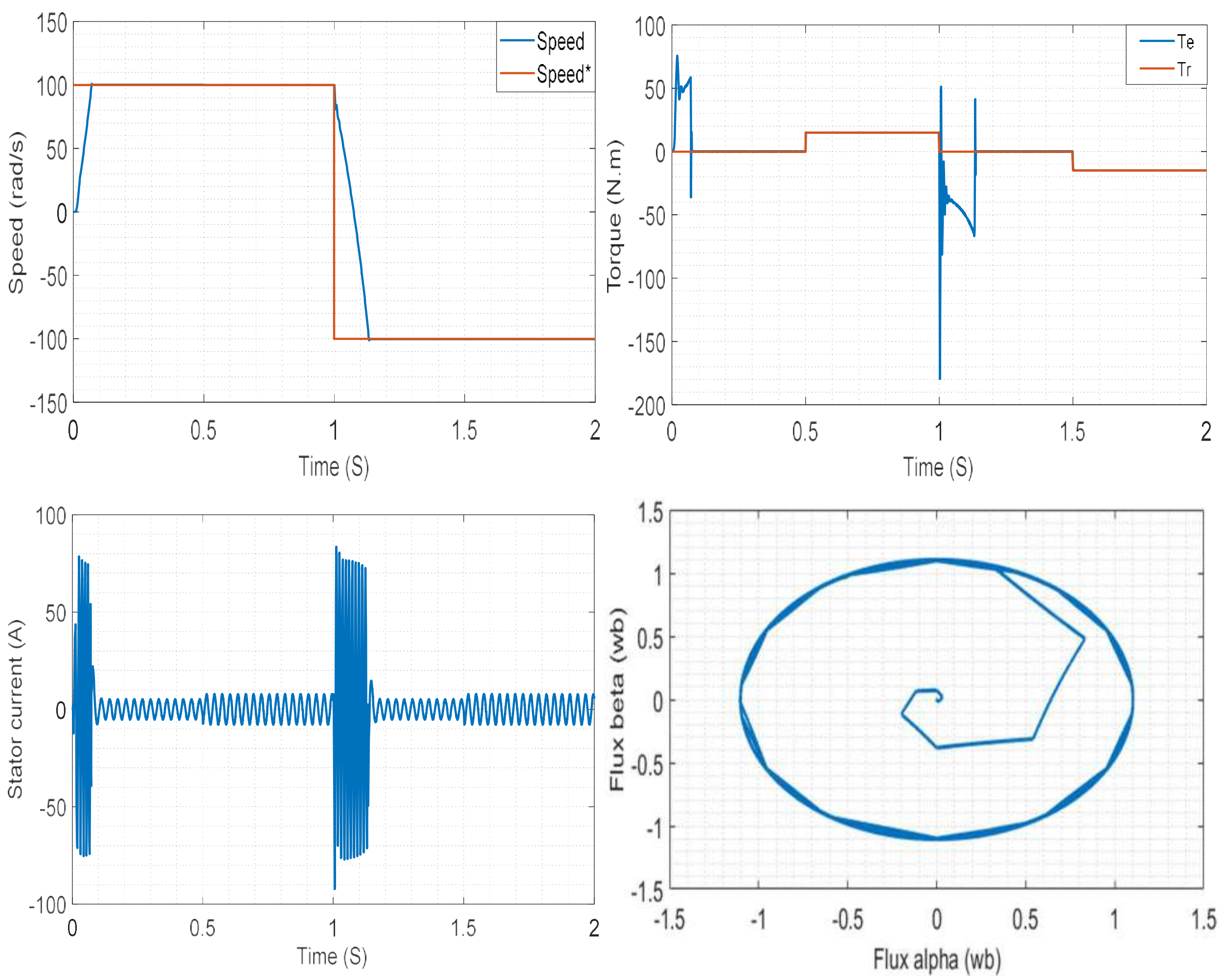

Fig. IV.10: DTC-IM dynamic response under ±100 rad/s speed reference.

The simulation results demonstrate the effectiveness of the DTC strategy for the induction motor operating at reference speeds of ±100 rad/s, Fig. IV.10. The speed response exhibits fast dynamics with accurate tracking and negligible steady-state error, and the reversal from positive to negative speed at t=1 s is achieved rapidly.

The electromagnetic torque exhibits high transient peaks during startup and speed reversal due the high torque demand during acceleration and braking, along with noticeable ripples characteristic of conventional DTC. Similarly, the stator current presents high transient amplitudes before becoming nearly sinusoidal in steady state. In addition, the stator flux trajectory in the (α−β) plane remains approximately circular, confirming effective flux regulation despite transient distortions. Overall, the results confirm that the DTC technique provides fast response, accurate speed tracking, and satisfactory performance under sudden speed reversals.

IV.5.2 Performance DTC under 50 a -50 rad/s

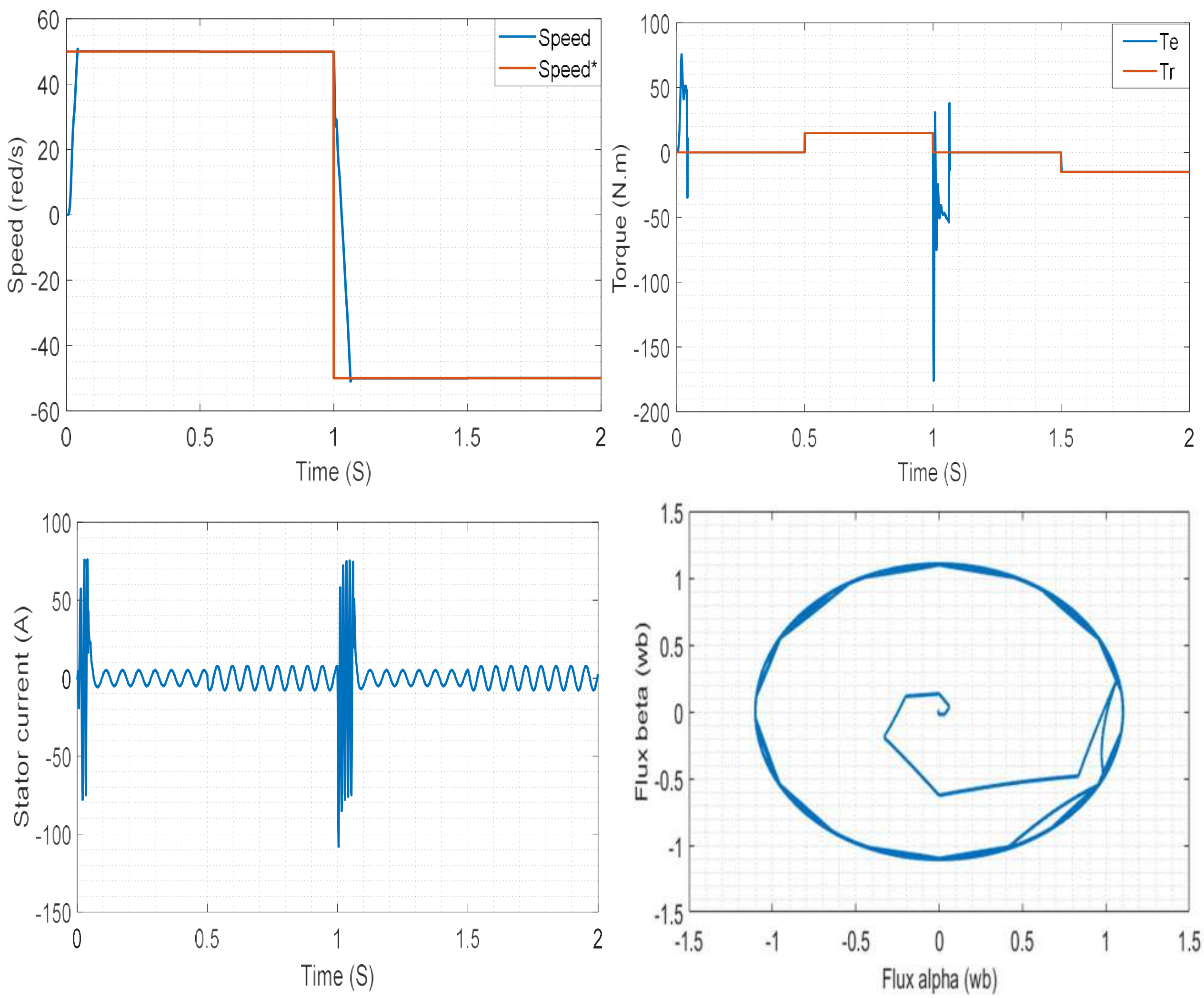

Fig. IV.11: DTC-IM dynamic response under ±50 rad/s speed reference.

The simulation results demonstrate the effectiveness of the DTC-IM control strategy for bidirectional speed tracking at reference values of ±50 rad/s, with fast dynamic response and negligible steady-state error, Fig. IV.11.

The electromagnetic torque presents transient peaks during startup and speed reversal, which is a normal behavior in DTC systems due to sudden changes in reference conditions. Similarly, the stator current exhibits high transient values during switching intervals before stabilizing with reduced steady-state ripple. The flux trajectory in the α-β plane remains nearly circular, confirming proper flux regulation and effective decoupling between torque and flux.

Overall, the results validate the system's ability to ensure fast response, stable operation, and accurate speed tracking under dynamic operating conditions.

IV.5.3 Comparative Analysis under Variable Irradiance (PI vs. PI-GTO)

Fig. IV.13 presents the overall performance of the PVWPS under varying solar irradiance conditions (Fig.IV.12) using different control strategies.

The PV array power obtained via the AD-INC-MPPT technique (Fig. IV.13.a) demonstrates efficient and accurate tracking of the MPP, even under continuous and rapid irradiance fluctuations. Compared with the conventional DTC strategy, which exhibits noticeable power oscillations under the same operating conditions, the proposed PI-GTO-DTC approach significantly enhances system performance by reducing power fluctuations and improving the overall dynamic response of the PV generation subsystem.

The rotor speed response shown in Fig. IV.13(b), obtained using a speed reference derived from the maximum PV power tracked, confirms that the PI-GTO controller achieves accurate and stable speed tracking with considerably reduced oscillations compared to the classical PI-DTC approach. This improvement in speed regulation directly contributes to enhancing the hydraulic behavior of the system, as illustrated in Fig. IV.13.c, where the smoother rotor speed leads to a more stable, continuous, and reliable water flow, improving the overall performance of the pumping process.

Regarding the electromagnetic torque behavior depicted in Fig. IV.13.d, the proposed PI-GTO-DTC strategy effectively mitigates torque ripples under varying solar irradiance conditions, ensuring smoother motor operation and improving energy conversion efficiency. In addition, the stator current waveform shown in Fig. IV.13.e under the proposed control becomes nearly sinusoidal, with a significant reduction in current ripples and waveform distortions, whereas the conventional DTC strategy exhibits pronounced distortions and oscillatory behavior.

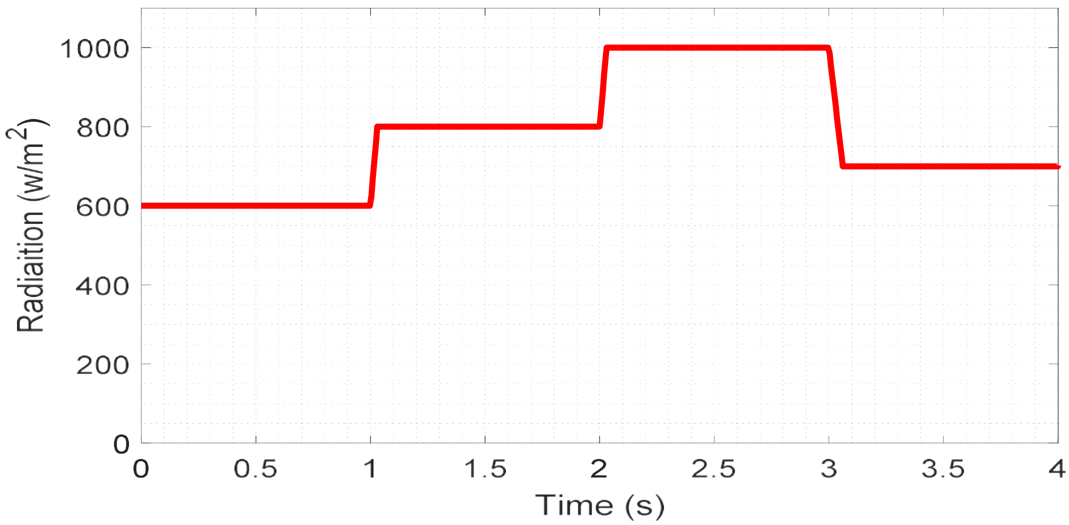

Fig. IV.12: Solar irradiance profile (W/m²)

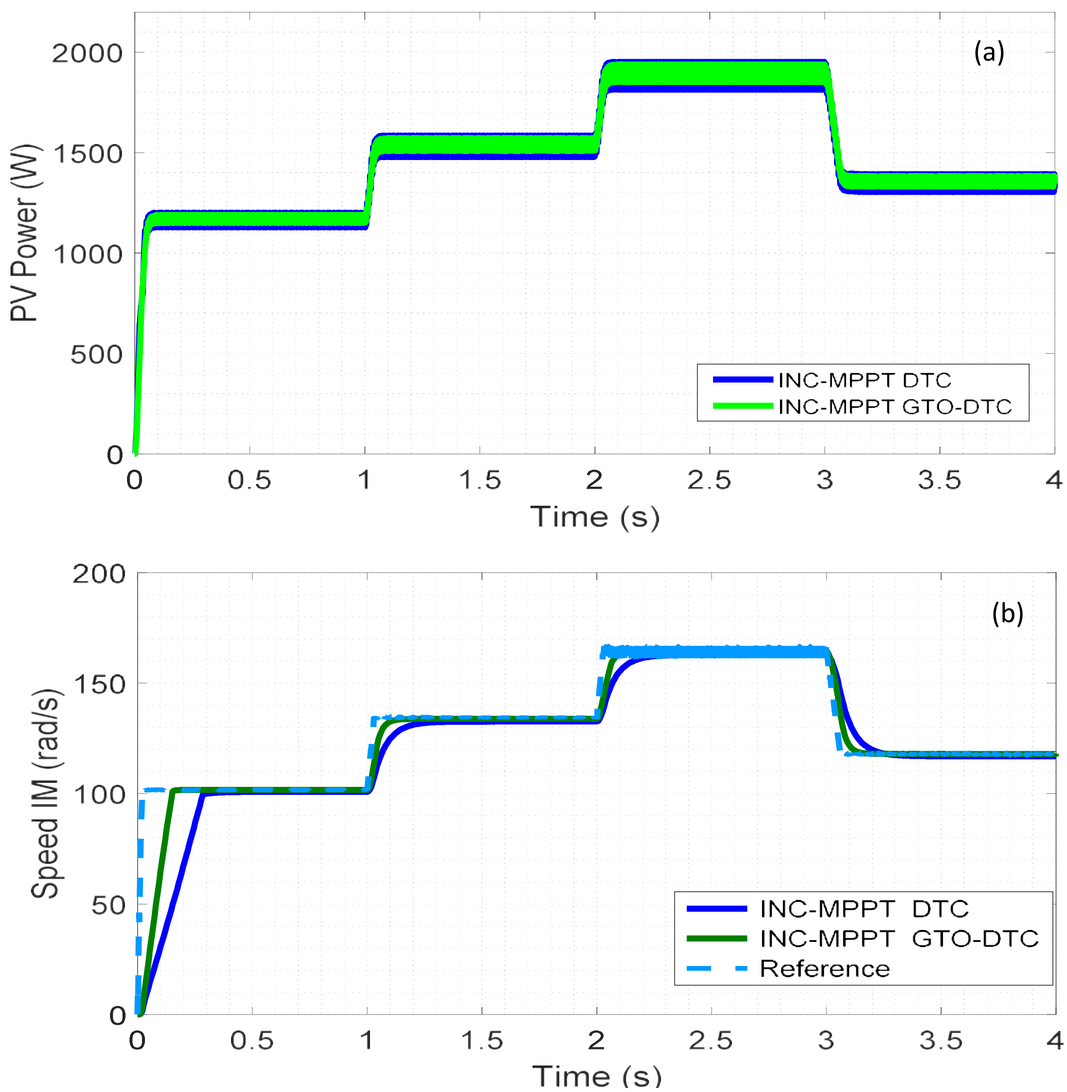

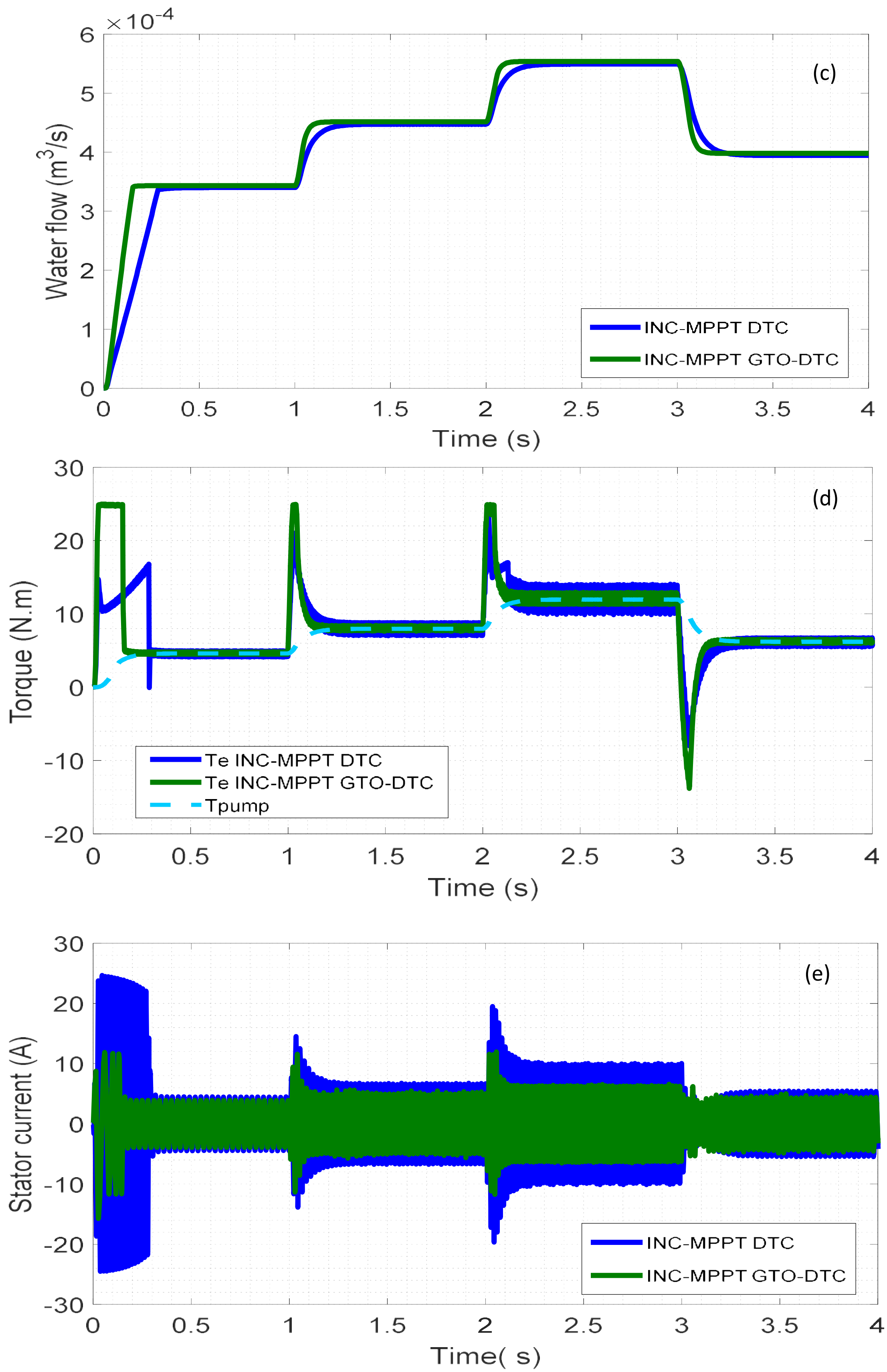

Fig.IV.13: PVWPS performance with AD-INC-MPPT technique under DTC, and GTO-DTC control strategies: (a) PV power, (b) Speed, (c) Water flow, (d) Torque, and (e) Stator current.

IV.6 Conclusion

This chapter presented the design and implementation of the proposed PI-GTO-DTC for photovoltaic water pumping system. The fundamental principles of DTC, including flux and torque estimation, hysteresis control, and switching table selection, were first discussed. Subsequently, the GTO algorithm was introduced as an optimization technique for tuning the PI controller gains in order to enhance the dynamic and steady-state performance of the induction motor drive. The simulation results demonstrated that the proposed PI-GTO-DTC strategy significantly improves the overall system performance compared with the conventional PI-DTC approach. The optimized controller ensured faster speed tracking, reduced torque and flux ripples, improved stator current quality, and enhanced robustness under variable solar irradiance conditions. Moreover, the smoother dynamic response contributed to more stable hydraulic operation and improved pumping reliability.

General Conclusion

This work addressed the modeling and performance enhancement of a photovoltaic water pumping system driven by an induction motor, with the objective of improving energy efficiency, dynamic response, and system robustness under variable environmental conditions. The study was structured into four main chapters covering system background, mathematical modeling, and advanced control design.

First, the photovoltaic generation subsystem was modeled, including the PV array and DC–DC boost converter. Several MPPT techniques were investigated and compared, namely P&O, INC, and AD-INC. The results demonstrated that the AD-INC method provides superior performance in terms of tracking accuracy, faster convergence, reduced oscillations, and improved energy harvesting under varying irradiance and temperature conditions. Second, detailed mathematical models of the main components of the pumping system were developed, including the induction motor, centrifugal pump, and voltage source inverter. The induction motor was represented in the d–q reference frame to accurately capture its dynamic behavior, while the pump model described the nonlinear hydraulic relationship between flow rate, head, and speed. These models provided a solid foundation for system analysis and control design. Third, an improved control strategy based on Direct Torque Control (DTC) was developed to enhance the performance of the motor drive. To overcome the limitations of conventional DTC, a Proportional–Integral (PI) controller optimized using the Gorilla Troops Optimizer (GTO) was introduced. The proposed PI-GTO-DTC approach effectively minimized speed tracking error and torque ripples while improving the overall stability of the drive system. Finally, simulation results carried out in *MATLAB/Simulink* confirmed the effectiveness of the proposed approach under different operating conditions, including speed reversals and variations in solar irradiance. The results showed significant improvements in dynamic response, torque and flux ripple reduction, stator current quality, and system robustness compared to conventional control methods. The combination of AD-INC MPPT with PI-GTO-based DTC further enhanced the overall efficiency and reliability of the PVWPS.

In conclusion, the proposed modeling and control framework provides a comprehensive and effective solution for photovoltaic water pumping systems. It ensures improved energy extraction, better electromechanical performance, and reliable operation under real environmental variations, making it suitable for sustainable water pumping applications in remote and agricultural areas.

Bibliography

[1]. Benghanem M, Haddad S, Alzahrani A, Mellit A, Almohamadi H, Khushaim M, Aida MS. Evaluation of the Performance of Polycrystalline and Monocrystalline PV Technologies in a Hot and Arid Region: An Experimental Analysis. *Sustainability*. 2023; 15(20):14831.

[2]. Alami, A.H. et al. (2023). Second-Generation Photovoltaics: Thin-Film Technologies. In: Alami, A.H. (eds) PV Technology and Manufacturing. Advances in Science, Technology & Innovation. Springer, Cham.

[3]. Chava, V.S.N., Sreenivasan, S.T. (2022). Material and Process-Related Contaminants in Solar Photovoltaics: Key Issues, and Future Prospects. In: P. Singh, S., Agarwal, A.K., Gupta, T., Maliyekkal, S.M. (eds) New Trends in Emerging Environmental Contaminants. Energy, Environment, and Sustainability. Springer, Singapore.

[4]. R. Bradai et al., Experimental assessment of new fast MPPT algorithm for PV systems under non-uniform irradiance conditions, Appl. Energy, vol. 199, pp. 416–429, 2017.

[5]. Duffie, J.A., & Beckman, W.A. Solar Engineering of Thermal Processes. 4th Edition, John Wiley 2013.

[6]. Villalva, M. G., Gazoli, J. R., & Filho, E. R. (2009). Comprehensive approach to modeling and simulation of photovoltaic arrays. IEEE Transactions on Power Electronics, 24(5), 1198–1208.

[7]. Abad, Lahlou, Tamalouzt, Salah, Djermouni, Kamel, Mekhilef, Saad, Belkhier, Youcef, Analytical Modeling of Photovoltaic Systems Under Partial Shading Conditions Incorporating Bypass and Blocking Diodes Influence, International Journal of Energy Research, 2025, 3384091, 21 pages, 2025. https://doi.org/10.1155/er/3384091

[8]. Messenger, R.A., & Abtahi, H. (2024). Photovoltaic Systems Engineering (5th ed.). CRC Press. https://doi.org/10.1201/9781003470892

[9]. Masters, G. M. Renewable and Efficient Electric Power Systems. 2004, John Wiley & Sons, Inc. DOI:10.1002/0471668826

[10]. Xiao, W., El Moursi, M.S., Khan, O. and Infield, D. (2016), Review of grid-tied converter topologies used in photovoltaic systems. IET Renewable Power Generation, 10: 1543-1551. https://doi.org/10.1049/iet-rpg.2015.0521

[11]. Bagalini V, Zhao BY, Wang RZ, Desideri U. Solar PV-Battery-Electric Grid-Based Energy System for Residential Applications: System Configuration and Viability. Research (Wash D C). 2019: 3838603. doi: 10.34133/2019/3838603.

[12]. Taghizad-Tavana K, Esmaeel Nezhad A, Hagh MT, Canani A, Safari A. Hybrid Renewable Energy Systems for Off-Grid Electrification: A Comprehensive Review of Storage Technologies, Metaheuristic Optimization Approaches and Key Challenges. *Eng*. 2025; 6(11):309. https://doi.org/10.3390/eng6110309

[13]. S. Mekhilef, R. Saidur, and A. Safari, “A review on solar energy use in industries,” Renewable and Sustainable Energy Reviews, vol. 15, no. 4, pp. 1777–1790, 2011.

[14]. K. Deb, Optimization for Engineering Design: Algorithms and Examples. New Delhi, India: Prentice-Hall, 2012.

[15]. R. W. Erickson and D. Maksimović, Fundamentals of Power Electronics, 2nd ed. Boston, USA: Springer, 2001.

[16]. N. Femia, G. Petrone, G. Spagnuolo, and M. Vitelli, Power Electronics and Control Techniques for Maximum Energy Harvesting in Photovoltaic Systems. Boca Raton, USA: CRC Press, 2012.

[17]. Chaibi, Y., Allouhi, A., Salhi, M. et al. Annual performance analysis of different maximum power point tracking techniques used in photovoltaic systems. Prot Control Mod Power Syst 4, 15 (2019). https://doi.org/10.1186/s41601-019-0129-1

[18]. Ramdan B Koad, An improved Maximum Power Point Tracking For PV System, Doctor of Philosophy, Department of Electronic and Computer Engineering, College of Engineering, Design and Physical Sciences, Brunel University London, January 2017.

[19]. Nacer Kouider M'Sirdi, Abdelhamid Rabhi, Bechara Nehme. The VSAS approch gives the best MPPT for solar energy sources (RES). Journal of Renewable Energy and Sustainable Development (RESD) , 2015, 1 (1), pp.60/71.

[20]. K. H. Hussein, I. Muta, T. Hoshino, and M. Osakada, Maximum photovoltaic power tracking: An algorithm for rapidly changing atmospheric conditions, Proc. IEE—Generation, Transmission, Distribution, vol.142, no. 1, pp. 59–64, Jan. 1995.

[21]. Hairul Nissah Zainudin, Saad Mekhilef, Comparison Study of Maximum Power Point Tracker Techniques for PV Systems, Proc. 14th international middle east power system conference (MMEPCON"10), Cairo University, Egypt, 2010, 750-755.

[22]. M. A. Elgendy, B. Zahawi, and D. J. Atkinson, "Assessment of perturb and observe MPPT algorithm implementation techniques for PV pumping applications," IEEE Transactions on Sustainable Energy, vol. 3, no. 1, pp. 21–33, Jan. 2012

[23]. Safari, A., & Mekhilef, S. (2011). Simulation and hardware implementation of incremental conductance MPPT with direct control method using Cuk converter. IEEE Transactions on Industrial Electronics, 58(4), 1154–1161

[24]. R. Krishnan, Electric Motor Drives: Modeling, Analysis, and Control. Upper Saddle River, NJ, USA: Prentice Hall, 2001.

[25]. P. C. Krause, O. Wasynczuk, S. D. Sudhoff, and S. Pekarek, Analysis of Electric Machinery and Drive Systems, 3rd ed. Hoboken, NJ, USA: Wiley-IEEE Press, 2013.

[26]. Lesenne J, Notel F. Introduction to in-depth electrical engineering, Technique et documentation. Paris, France; 1981.

[27]. Hamidat, A., & Benyoucef, B. (2009). Systematic procedures for sizing photovoltaic pumping system, using water tank storage. Energy Policy, 37(4), 1489–1501.

[28]. P. Sharma and V. Agarwal, "Exact maximum power point tracking of grid-connected partially shaded PV source using current compensation concept," IEEE Transactions on Power Electronics, vol. 29, no. 9, pp. 4684–4692, Sep. 2014.

[29]. P. Vas, Sensorless Vector and Direct Torque Control, Oxford University Press, 1998.

[30]. Wang, L.; Gao, Y. A Novel Strategy of Direct Torque Control for PMSM drive Reducing Ripple in Torque and Flux. In Proceedings of the 2007 IEEE International Electric Machines & Drives Conference, Antalya, Turkey, 3–5 May 2007; Vo1ume 1, pp. 403–406.

[31]. A. Mossa, M., Echeikh, H., Diab, A. A. Z., Haes Alhelou, H., & Siano, P. (2021). Comparative Study of Hysteresis Controller, Resonant Controller and Direct Torque Control of Five-Phase IM under Open-Phase Fault Operation. *Energies*, *14*(5), 1317.

[32]. Hugo, G.; Mario, D.; Federico, B.; Blas, B.; Sergio, T. Speed control of five-phase induction motors with integrated open-phase fault operation using model-based predictive current control techniques. *IEEE Trans. Ind. Electron.* 2014, *61*, 4474–4484.

[33]. Kechida, R., Gacem, A., Romdhane, M., Naoui, M., Almalaq, Y., Alturki, M., Albaker, A., & Guesmi, T. (2024). High-efficiency predictive torque control of induction motors in PV water pumping using GTO-optimized PI controller. Scientific Reports, 14.

[34]. A. Abdollahzadeh, B. Gharehchopogh, and S. Mirjalili, "African vultures optimization algorithm: A new nature-inspired metaheuristic algorithm for global optimization problems," Computers & Industrial Engineering, vol. 158, 2021.

Appendix

A. Induction Motor Parameters :

IM		Values
Nominal power (P)	[KW]	4
Rated speed(Ω)	[rpm]	1420
Nominal frequency (f)	[Hz]	50
Stator resistor (Rs)	[Ω]	9.81
Rotor resistor (Rr)	[Ω]	5.3
Stator inductor (Ls)	[H]	0.277
Rotor inductor (Lr)	[H]	0.277
Mutual inductor (M)	[H]	0.258
Number of pole pairs		2

B. Parameter Values of the Boost Converter:

Parameters	Values
V_{dc}	600 V
C_1	500 µF
C_2	700 µF
L	3.5 mH

C. PV Parameters :

Parameters of the PV		Values
Maximum power (P_{mpp})	[W]	325
Maximum current (I_{mpp})	[A]	9.01
Maximum voltage (V_{mpp})	[V]	36.07
Open circuit voltage (V_{oc})	[V]	45.35
Short circuit current (I_{cc})	[A]	9.38